"Quasidirect" observations of cosmic-ray primaries in the energy region 10^{12}–10^{14} eV

Yasuhiro Kawamura, Hideya Matsutani, Hirotada Nanjyo,
Katsuya Teraoka, and Kimio Toda
Department of Physics, Hirosaki University, Hirosaki, Japan

Masakatsu Ichimura, Keisuke Kirii, Tadashi Kobayashi, Yasuo Niihori, Toru Shibata,
Kazuo Shibuta, and Yasuko Yoshizumi
Department of Physics, Aoyama Gakuin University, Tokyo, Japan

We have exposed an emulsion chamber at a level of 32.8 g/cm^2 for ~ 30 h, and detected ~ 800 showers on x-ray films (Fuji No. 200 type). Among these, ~ 200 primaries ($\sum E_\gamma \geq 2$ TeV, $\theta < 75°$) were identified by tracing back through successive plates of nuclear emulsion. On the basis of these primaries, we obtain $I_p(\geq E_0) = 1.02 \times 10^{-5} [E_0/(1 \text{ TeV})]^{-1.82 \pm 0.13}$ (cm^2 sec sr)$^{-1}$ in the region $5 \lesssim E_0 \lesssim 100$ TeV for proton primaries, and $I_\alpha(\geq E_0) = 6.50 \times 10^{-7} [E_0/(1 \text{ TeV/nucleon})]^{-1.75 \pm 0.15}$ (cm^2 sec sr)$^{-1}$ in the region $3 \lesssim E_0 \lesssim 10$ TeV/nucleon for α primaries. We observed also many atmospheric secondary γ rays, which cover the energy region 2–80 TeV. The γ-ray spectrum is a rather smooth continuation of that obtained by Nishimura *et al.* in the region 0.2–2 TeV. The higher-energy part of our flux, however, cannot be reproduced by the atmospheric nuclear interaction of the primary protons and α particles alone, indicating that, for energies $\gtrsim 10^{14}$ eV/nucleus, the contribution of heavier primaries becomes significant, and that the latter flux may very well become comparable with the proton flux somewhere between 10^{14} and 10^{15} eV/nucleus. This indication is consistent with the iron flux obtained directly by the present experiment, though poor statistics preclude a conclusive result.

I. INTRODUCTION

It is extremely important for both high-energy astrophysics and high-energy particle physics to determine *directly* the chemical composition and the energy spectrum of primary cosmic rays in the energy region 10^{14}–10^{16} eV. In particular, the energy spectra of the individual components in the region $\gtrsim 10^{15}$ eV will bring us valuable information about the origin of cosmic rays as well as their acceleration mechanism. Further, this information also provides a meaningful normalization point against indirect data such as extensive air showers (EAS's) and/or atmospheric muons.

Although direct observations reach energies at ~ 100 TeV/nucleus at present, a unified view is still unavailable. For instance, the Moscow groups (Grigorov *et al.*[1] and Abulova *et al.*[2]) report a proton spectrum whose integral spectral index changes from -1.8 to -2.2 in the energy region $\gtrsim 5$ TeV. The Japanese-American Cooperative Emulsion Experiment[3] (JACEE) gives a spectrum up to ~ 100 TeV, which is in accord with the extrapolation with an index -1.8 from that at ~ 1 TeV obtained by Ryan, Ormes, and Balasubrahmanyan.[4] The Fuji-Kanbala group[5] (emulsion-chamber experiment at mountain level) and several EAS groups[6] point out that the iron component exceeds the proton component in the region $\gtrsim 10^{14}$ eV/nucleus, while JACEE (Ref. 7) reports no significant change in the iron/proton ratio, at least up to $\sim 10^{14}$ eV/nucleus. Direct data,[8] obtained most recently by a space-borne experiment, indicate an increase in the relative iron abundance up to ~ 100 TeV. Obviously,

there still exist discrepancies on the primary composition and spectra in the region 10^{12}–10^{14} eV/nucleus among the researchers. Therefore it is very desirable to get better statistics of the direct data in the higher-energy region $\gtrsim 10^{14}$ eV/nucleus.

Simple scaling up of a passive particle detector such as an emulsion chamber, however, will not be enough for our present purpose, because we will have to solve some technical problems at the same time. For instance, we will have to overcome the difficulty in energy estimation of heavy primaries with Lorentz factors $\gtrsim 10^5$. The secondaries arising from a local nuclear collision within the apparatus have such small emission angles that the energy estimation based on the latter would need a spacing between the vertex and the angle measurement layer of at least several meters. The method based on the measurement of $\sum E_\gamma$, the energy dissipated in the form of electron showers, on the other hand, would need at least 12-radiation-length-thick absorber layers ($\simeq 6$ cm Pb, see Fig. 9 below) to detect the shower maximum in the region $\sum E_\gamma \gtrsim 100$ TeV. These requirements are hard to satisfy in ordinary balloon-borne apparata.

We have proposed the possibility of "quasidirect" observations at relatively low levels, about several tens of g/cm^2, the details of which have already been presented in Ref. 9.

Naturally the data obtained by "purely direct" observations are far superior to those by any other "impure" method. One should, however, keep in mind that even for "purely direct" observations, the experimental results obtained by passive detectors are closely related to the

model of nuclear interactions, particularly those of nucleus-nucleus collisions, when calculating both detection efficiency and conversion factors from the secondary-energy sum $\sum E_\pi$ to the primary energy E_0.

We should comment on the capabilities of balloons. Exposures at modest elevation heights have disadvantages due to the contaminating secondary cosmic rays arising from the atmospheric nuclear interactions and, therefore, it is desirable that the observation levels be as high as possible.

There exists, however, the following relation between the total payload W and the atmospheric depth t of the observation level:

$$t \propto \frac{W}{V} \, ,$$

where V is the balloon volume. This means, typically, that we can launch a 500-kg apparatus at a height of 50 millibars using a balloon whose volume is more or less the same as that of a balloon which lifts 50 kg up to 5 millibars.

We therefore performed a balloon experiment at a modest elevation level in May 1987, focusing mainly on the evaluation of the quality of "quasidirect" observations and the technical developments for light-weight chambers. Let us summarize our experimental objectives more explicitly in the following.

(a) We obtain the proton spectrum in the region $\gtrsim 5$ TeV, and understand the reason for the contradictory results among the researchers mentioned above.

(b) With the use of the data of atmospheric γ rays and γ bundles, we get some crude information on the primary composition in the region $10^{13}-10^{15}$ eV/nucleus.

(c) We observe hadron bundles (fragment nuclei, α's, nucleons, and $\pi^\pm$'s) originating from the fragments of heavy primaries, and estimate the charges and energies of the primary nuclei which have generated them, according to the method described in Ref. 9.

(d) For the energy determination of the cascade showers initiated by γ rays as well as protons and heavy primaries, we have prepared a handy tool—a microcomputer software package. We check, by simulation, the accuracy and precision, as well as the computational efficiency, of our present energy determination method.

(e) We use new types of sensitive materials such as screen-type x-ray films and thermoluminescence sheets in order to develop a chamber somewhat different from the usual type containing a calorimeter of considerable weight.

For (a), since the contamination of cosmic-ray secondaries ($\pi^\pm$, nucleon) is significant at our observation level of 32.8 g/cm^2, we estimate the proton spectrum in an analytical way summarized in Sec. IV C and Appendix B, and eliminate the background carefully, referring also to the result of simulation calculations. Further, both the detection efficiency and the conversion of observed energy to primary energy are extremely important in obtaining the absolute intensity of primaries. Nevertheless, previous workers with direct observation data have not always paid enough attention to these numerical procedures. In the present work, we detail these processes in

Sec. IV and Appendix E, particularly on the fluctuation of observed electron shower energy.

For (b), we show in Sec. V B that it is possible to deduce valuable information on primary composition in the energy region $10^{12}-10^{15}$ eV from the γ-ray (and γ-bundle) flux, even though it is not "purely direct" data.

For (c), unfortunately, we did not detect hadron bundles (p, n, α) in the present observation. We can, however, speculate on the upper limit of the iron flux in the region $\gtrsim 10^{12}$ eV/nucleon, as discussed in Sec. VI.

For (d), we apply the method used for the general type of balloon-borne emulsion chamber, as discussed in detail in Ref. 10, for the present experiment, and show explicitly, in Sec. III, the efficiency of our energy determination system, and the accuracy and precision of the energy determined in Sec. III.

For (e), we briefly point out the possibility of these sensitive materials in Secs. II B and II C. Section VI is reserved for discussions on the comparison of our data with others, including both direct and indirect observations.

II. EXPERIMENTAL PROCEDURE

A. Chamber structure and flight situation

As shown in Fig. 1, our chamber consists of two parts: a target layer (A, B) and a shower calorimeter (C, D).
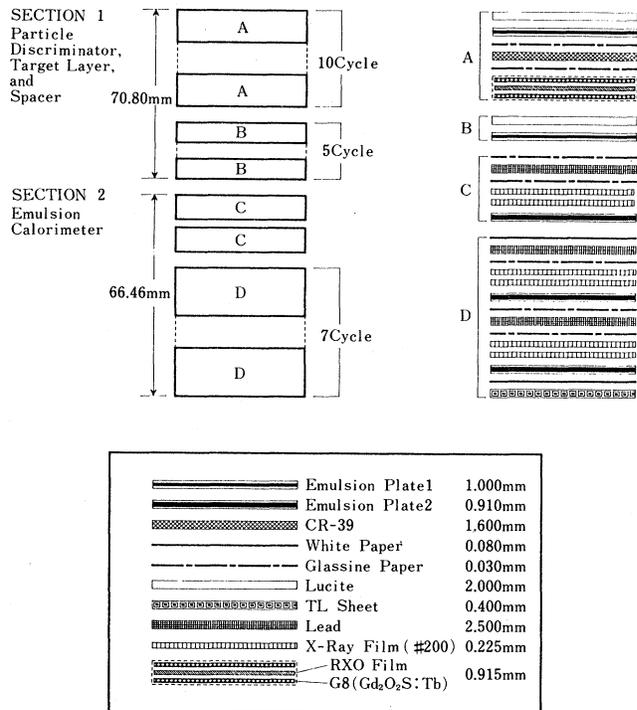

FIG. 1. Schematic view of the present chamber structure and the detail of materials inserted.

TABLE I. Processing method for nuclear emulsion and x-ray films (RXO type and No. 200 type).

Sensitive material	Presoak (min)	Developing (min)	Stop (min)	Fix (min)
Fuji RXO film		15	3	15
Fuji No. 200 film		22	5	15
Fuji nuclear emulsion plate	10	25	10	60–90

The former serves not only as a nuclear target, but also as a charge discriminator for primary projectiles and as a spacer for the resolution of the secondaries produced. Each nuclear plate inserted in the target part is coated with 100-μm-thick Fuji 2F nuclear emulsion on the top, and with 100-μm-thick Fuji 7B nuclear emulsion on the bottom. Fuji 2F records particle tracks of ionization greater than 10 times that of relativistic electrons. This means that it records only the tracks of heavy primaries of $Z \gtrsim 4$ at the geomagnetic latitude of Sanriku flight station in Japan. Therefore it offers us the advantage of quickly detecting the heavy primary tracks. Fuji 7B, on the other hand, records all the particle tracks, including those that are not recorded in Fuji 2F—protons, α's, and electron showers.

In addition, we insert a solid track detector (CR-39) and screen-type x-ray film (hereafter called RXO film) together so that heavy tracks ($Z \gtrsim 6$) are detected quickly by the naked eye, and their charges are determined easily. RXO film was recently developed by Nishimura et al.[11] in order to reduce the detection threshold energy of primary electrons, and is known to be sensitive also for heavy tracks as well as jet showers.

The shower calorimeter is composed of sandwiches of sensitive materials (nuclear-emulsion plate and high-sensitivity x-ray film) and lead plates of 2.5 mm thickness. The nuclear emulsion plates inserted there are coated with high-sensitivity nuclear emulsion of 55 μm thickness (Fuji 7B type) on both sides.

The area of one unit of the chamber is 40×50 cm^2, and the total thickness is 13.7 cm, corresponding to 0.42 collision mean free path for proton, or 7.84 radiation length.
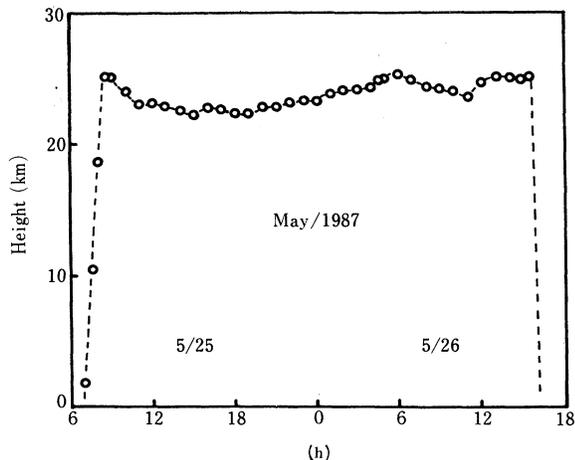
We exposed two units of this type of chamber. We launched these chambers on 25 May 1987 from Sanriku Balloon Flight Center, Japan, and recovered them successfully off Ofunato. As shown in Fig. 2, level-flight time is more than 30 h and the average level reached is 23.8 km (32.8 g/cm^2).

B. Scanning and tracing of cosmic-ray showers

After the recovery of the chamber, we processed quickly the sensitive materials such as x-ray films, nuclear-emulsion plates, and CR-39. In Tables I and II, we summarize the processing methods for these materials.

Electron showers are recorded on high-sensitivity x-ray film (Fuji No. 200 type) as dark spots, which are easily detected by the naked eye for showers with energy larger than ~ 1 TeV. As pointed out by Nishimura et al.,[11] the threshold energy of shower detection is ~ 0.3 TeV with the use of RXO film, much lower than that in the case of No. 200-type film. In our chamber, however, the detection is performed as usual by the use of No. 200 type, since RXO films are inserted only in the target layer.

After the detection of shower spots on the x-ray films is

FIG. 2. Flight record of the present exposure.

TABLE II. Etching condition for CR-39. HCB is hexachlorobutadiene, IPP is diisopropyl peroxydicarbonate, and N-445 is 0.01% naugard 445 antioxidant.

Composition		Solution	Time (h)
CR-39	96.49%	80°C 7N NaOH	96
IPP	3.00%	(fresh)	
N-445	0.01%		
HCB	0.50%	80°C 7N NaOH	96
		(reused)	
CR-39	96.89%	80°C 7N NaOH	96
IPP	3.00%	(fresh)	
N-445	0.01%		
HCB	0.10%		
CR-39	96.99%	80°C 7N NaOH	24
IPP	3.00%	(fresh)	
N-445	0.01%		
		80°C 7N NaOH	24
		(reused)	
		80°C 7N NaOH	14
		(fresh)	

completed, we reproduce automatically cosmic-ray traces on a horizontal plane with use of a digitizer (the so-called mapping process). The efficiency of this auto-mapping system is summarized in Ref. 12.

After performing the mapping process, we must find each vertex point in order to identify its primary charge. We traced back each shower recorded through successive nuclear-emulsion plates with the use of a wide-view-type microscope (Chiyoda Opt. Co.). Tracing speed is ~ 1.5 event/person day on average.

C. Identification of the cosmic-ray projectile

Identification of the cosmic-ray projectile is performed with help of various kinds of sensitive materials: nuclear-emulsion plate, CR-39, and RXO film.

First, a γ ray is easily identified in 7B-type nuclear emulsion by tracing back the electron shower up to its original electron pair.

Second, for protons and α's, we take the distribution of the gap length L_g between the centers of two grain images recorded along their tracks,[13] the results of which are demonstrated in Fig. 3. The vertical axis represents the number of gaps of length (per 100 μm) not smaller than L_g. We have found that it follows an exponential law, $N(\geq L_g) = N_0 \exp(-aL_g)$, and the value of the constant a for an α track is nearly 4 times that for a proton track, as expected from their respective specific ionizations.
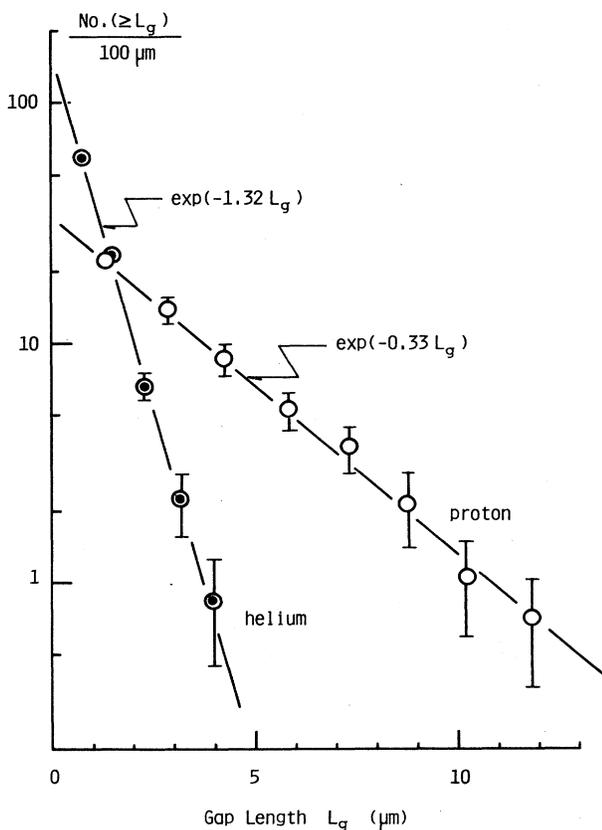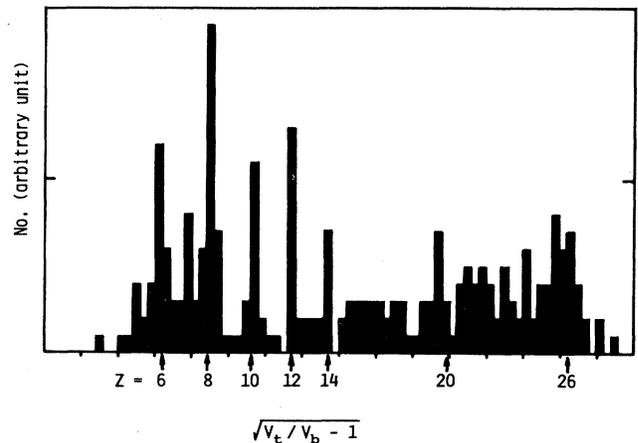

FIG. 4. Histogram of the square root of the reduced etch-rate ratio, $V_t/V_b - 1$, obtained by CR-39. Numerical values attached to the horizontal axis correspond to the track charge.

Third, heavy primaries ($\gtrsim$ CNO groups) are determined by three methods: δ-ray counting, etch-pit calibration, and spot-darkness measurements with the use of 7B-type nuclear emulsion, CR-39 and RXO film, respectively. The charge resolution with the use of RXO film is $\Delta Z = 1-2$ at this stage, not so satisfactory as the result ($\Delta Z \sim 0.5$) obtained by the other two methods, δ-ray counting and etch-pit calibration.

In Fig. 4 we present the distribution of the square root of the reduced etch-rate ratio[14] ($= V_t/V_b - 1$) obtained by CR-39, where V_t, V_b are track- and bulk-etch rate. Since a considerable part of iron primaries are broken into fragments in the upper atmosphere before arriving at our chamber, the iron-group peak is not sharp. On the other hand, we can see peaks of nuclei of carbon and oxygen.
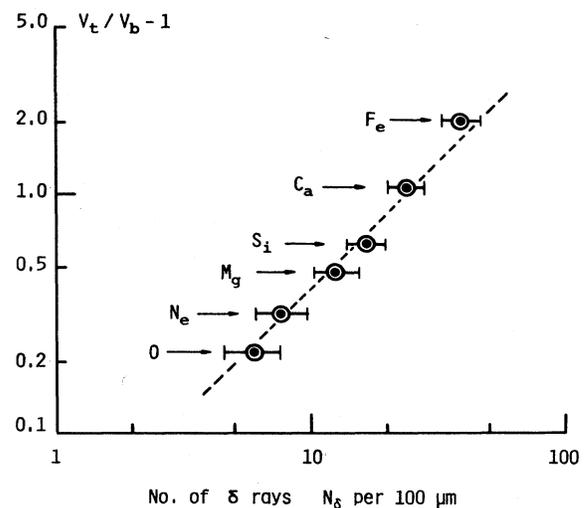
In Fig. 5 we present the correlation between the aver-

FIG. 3. Integral gap-length distribution per 100 μm of proton and α obtained by Fuji 7B-type nuclear emulsion.

FIG. 5. Correlation between the average number of δ rays per 100 μm and the reduced etch-rate ratio.

TABLE III. Summary of tracing results obtained by the present experiment.

Particle \ Chamber	A block (AOYAMA)	B block (HIROSAKI)	Total
γ ray	54	52	106
Proton	34	28	62
Helium	8	5	13
Light ($Z = 3-5$)	0	1	1
Medium ($Z = 6-8$)	1	2	3
Heavy ($Z = 10-15$)	1	0	1
Very heavy ($Z \gtrsim 20$)	0	2	2
Undefined	4	8	12
Subtotal	102	98	200
Not yet tracing	296	302	598
Total	398	400	798

age number of δ rays per 100 μm and the reduced etch-rate ratio, showing a nearly straight line at 45°. Charge determination with the use of RXO film will be reported elsewhere in the near future (preliminary analysis is given in Ref. 15).

In Table III we summarize the event list thus obtained,
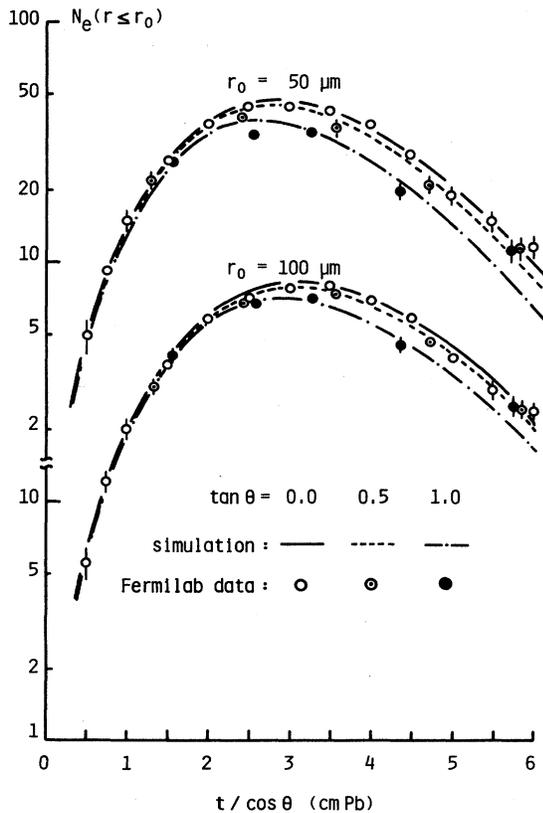

FIG. 6. Transitions of electron number obtained by Fermilab beam and simulation calculation in the case when the emulsion chamber is set with inclinations of 0°, 30°, and 45° against the incident electron beam.

where we present only events with shower energy larger than 2 TeV and zenith angle less than 75°.

III. ENERGY DETERMINATION

A. Transition of electron number

We have performed extensive simulations of electron cascade showers for balloon-borne emulsion chamber projects, details of which are reported in Refs. 10 and 16. Here, we discuss only those features that are relevant to the present experiment.

The simulated cascade showers have proved to reproduce quite well the observed lateral distribution of electrons on any target planes, when the shower axes are nearly normal to the latter. For balloon-borne emulsion chambers, however, we will first have to check the reliability of our simulations for showers of large inclinations, since, at balloon altitudes, we record frequently the showers with large zenith angles in our chamber in which the photosensitive layers are set horizontally. For the check, we compared our calculations with Fermilab data obtained by Hotta et al.,[17] exposing the emulsion chamber with inclinations of 0°, 30°, and 45° to the Fermilab electron beam. In Fig. 6 we present both results, showing that our calculations reproduce the Fermilab data well.

In Fig. 7 we give examples of the theoretical shower curves for transition of electron number, the so-called "transition curves," initiated by a *single* γ ray (hereafter called e pair since the calculations are started from birth point of the electron pair) together with experimental data. These theoretical curves are obtained by the program package of Ref. 16, taking into account the present chamber structure (see Fig. 1).

Besides the above-mentioned transition curves, we prepare also those initiated by *composite* γ rays ($\pi^0 \rightarrow 2\gamma$) arising from two kinds of nuclear interactions, one from proton interaction and the other from iron (hereafter called proton jet and iron jet, respectively), including zenith-angle effects. For composite γ rays arising from a nuclear interaction of a nucleus ($Z = 2-25$) other than iron, we apply the "proportional-allotment method." We have constructed, for several typical sample energies, simulation cascade showers induced by nuclei of several sample mass numbers in the range $4 \le A \le 55$, and have found out that the shower energy $\sum E_\gamma^{(A)}$ induced by a nucleus of mass number A is reproduced by

$$\sum E_\gamma^{(A)} = (1-p) \sum E_\gamma^{(1)} + p \sum E_\gamma^{(56)} \qquad (1)$$

in good approximation, where $p = \ln A / \ln 56$, and $\sum E_\gamma^{(1)}$ and $\sum E_\gamma^{(56)}$ are the shower energies estimated on the assumptions that the showers were induced by a proton and an iron nucleus, respectively.

From the curves in Fig. 7, we get the relation between the maximum electron number N_{max} and $\sum E_\gamma$. Figure 8 shows the curves giving the above-mentioned relations for several typical fixed values of r (radius to count electron number). We also consider two more initial conditions, proton jet and iron jet. Then we can determine the energy $\sum E_\gamma$ with use of N_{max} obtained by fitting the theoretical transition curves (Fig. 7) to experimental data.
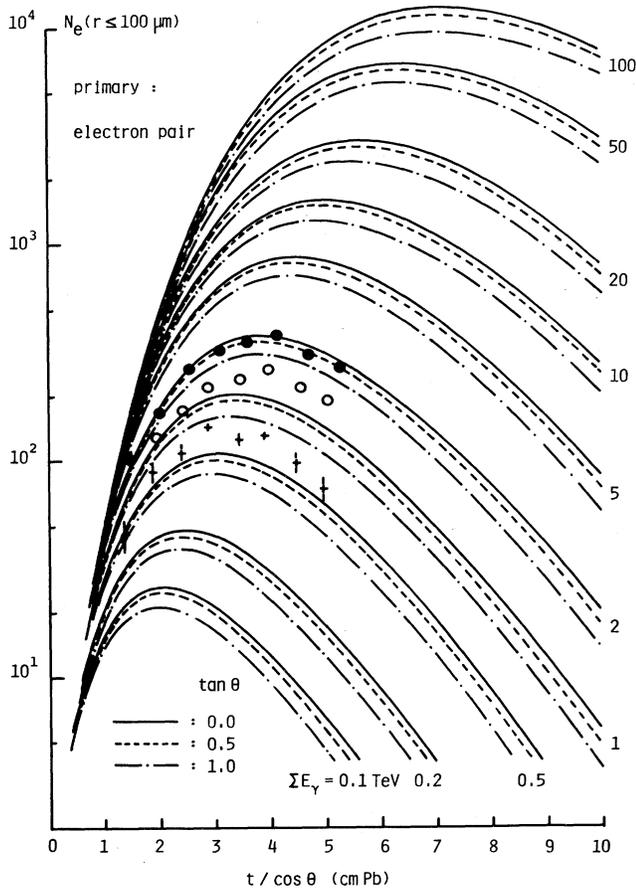
FIG. 7. Theoretical transition curves of electron number in the case of *e*-pair incidence corresponding to the present chamber structure (see Fig. 1). Examples of experimental data are also plotted.

FIG. 8. Relationship between energy flow released into γ rays, $\sum E_\gamma$, and the maximum electron number N_{max} for three incidences, *e* pair, proton jet, and iron jet.

As found in Fig. 8, the difference between *e* pairs and proton jets is rather small over a wide energy range, while N_{max} in the case of iron jets deviates significantly from the above two for small counting radii (say, $\lesssim 50$ μm), particularly in the lower-energy region $\lesssim 10$ TeV. The errors inherent in Fig. 8 are discussed in Sec. III D.

B. Transition of spot darkness on x-ray film

The energy determination with the use of spot darkness on high-sensitivity x-ray film has been already established through emulsion-chamber experiments at mountain altitudes.[18] Its application to balloon-borne measurements is, however, not straightforward. Techniques to solve the problems are briefly presented in Ref. 10. We omit the details here and show only numerical results that are necessary for the present experiment.

In order to obtain the theoretical transition curves of the darkness of shower spot recorded on x-ray films, one has to convert the density of electron number into the optical darkness, taking into account the lateral distribution of electron shower particles which have been obtained by the simulation calculations (see Sec. III A and Ref. 10).
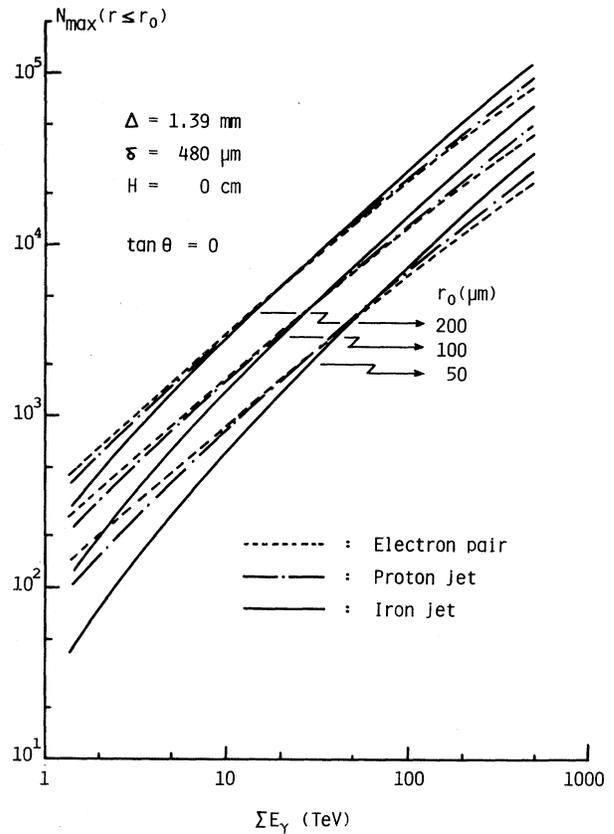
So we need a relation between ρ and D (ρ is the density of the electron number, D the darkness), the so-called "characteristic curve," which depends on the type of x-ray film.

In the present calculations, we modify the relation obtained by Ohta *et al.*[19] taking account of the different processing method (see Table I) as well as the zenith-angle effect,[20] in the following way:

$$D = D_0 \left[1 - \frac{1}{1+\alpha\rho} \right] , \qquad (2)$$

where ρ is electrons/cm^2, with

$$D_0 = 6.5 \text{ and } \alpha = 5.5 \times 10^{-8}/(\cos\theta)^{0.7} . \qquad (3)$$

In Figs. 9(a) and 9(b), we show the numerical results of the transition curves of spot darkness initiated by a proton jet and an iron jet, respectively, taking into account the present chamber structure. Several examples of experimental data ($\tan\theta = 0.3 - 2.0$) are plotted together.

From Fig. 9, we obtain the relation between the maximum of spot darkness D_{max} and $\sum E_\gamma$ in the cases of the proton-jet- and iron-jet-initiated showers, as shown in Fig. 10, and we also show those initiated by an *e* pair.

Since the numerical values D_0 and α given by Eq. (3) are somewhat affected by the experimental conditions

FIG. 10. Relationship between $\sum E_\gamma$ and maximum spot darkness D_{max}.
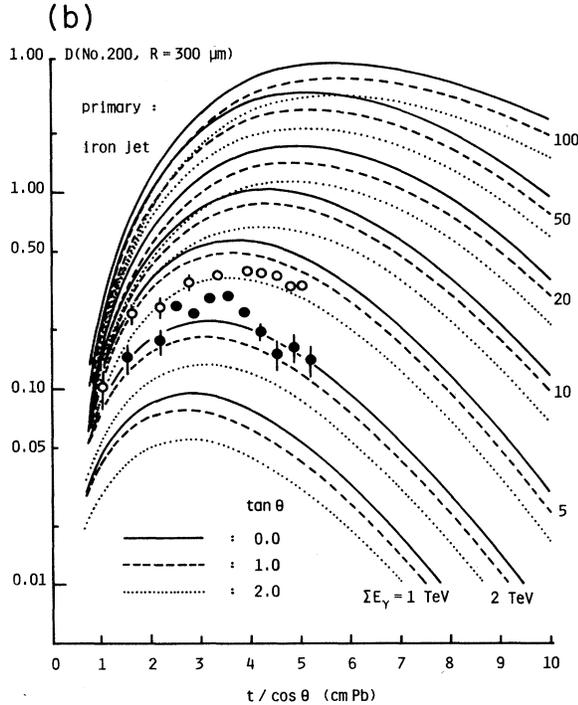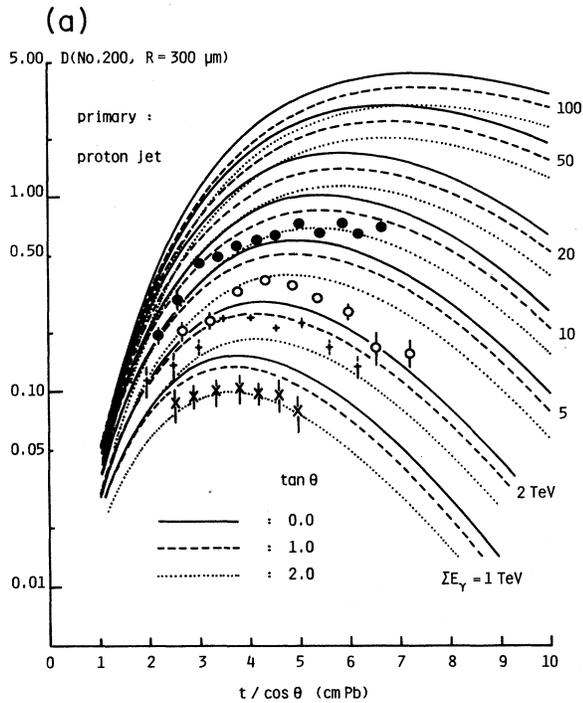

FIG. 9. Theoretical transition curves of spot darkness in the cases of (a) proton jet and (b) iron jet corresponding to the present chamber structure, where several examples of experimental data are plotted together.
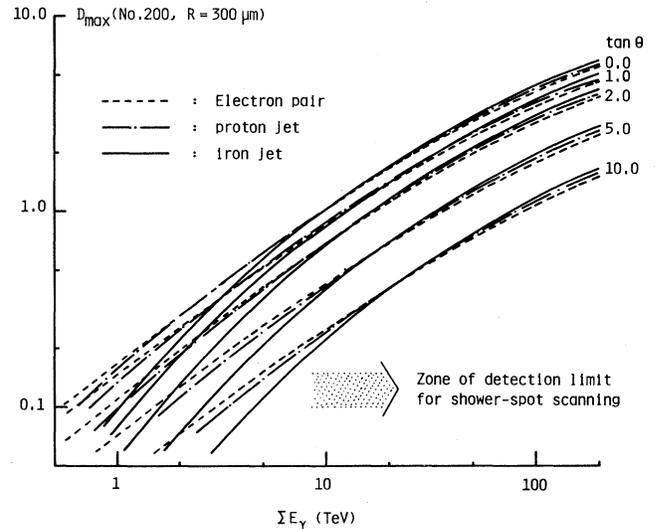
such as flight time (background radiation), processing method, and so on, the energy $\sum E_\gamma$ determined by Fig. 10 involves some uncertainty *in its absolute magnitude*. Therefore we must calibrate it absolutely through Fig. 8, obtained by counting electron number with the use of nuclear-emulsion plates. We found the calibration factor is ~ 1.0 as discussed later, telling that Eq. (2) accurately describes the present experimental condition.

C. Photodensitometer measurement

The spot darkness of the electron shower recorded on No. 200-type x-ray film depends, of course, on the slit size R of the photodensitometer, being approximately in inverse proportion to R. In the present measurement, the slit size (square type) is fixed to 300×300 μm^2. We always set the diagonal of the slit in the direction of the shower as shown in Fig. 11, and search the maximum darkness of the shower spot, moving the x-ray film along the onward direction. The theoretical curves mentioned in Sec. III B are of course calculated in the same way as the above condition of slit setting. In Appendix A we summarize the practical process of the energy determination with the use of photodensitometer.

Let us show two examples of transition curves obtained from the present experiment in Figs. 12(a) and 12(b), the former corresponding to the event with the highest energy in the present observation (incidence is γ ray with 85.6 TeV), and the latter to successive interactions of a proton.

In Fig. 13 we present the correlation between $E_{photometer}$ and E_{count}, the former obtained by the photometer and the latter by electron counting with the use of the nuclear emulsion plate. One finds a relation $E_{photometer} \simeq E_{count}$, confirming that Eq. (3) is appropriate, and telling us that no correction is necessary for the absolute calibration against spot darkness.
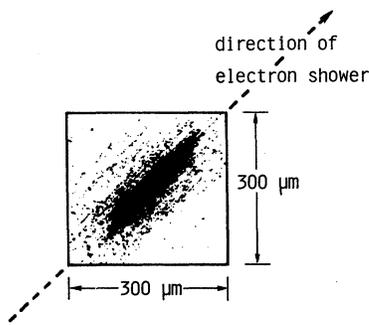
FIG. 11. Setting condition of photometer slit against shower-spot direction.

In Fig. 14 we give the scatter plot of $\sum E_\gamma$ vs $\tan\theta$ (θ is the zenith angle of shower) for all showers detected from the present observation. Since the detection limit of the electron shower is $D_{max} \simeq 0.1-0.15$, we can draw curves of detection limit from Fig. 10, showing that the experimental plots collimate in the expected area. As this indicates, the detection of showers with $\sum E_\gamma \gtrsim 2$ TeV and $\theta < 75°$ is unbiased, so that we use only these events for the analysis of the primary composition and its energy spectrum.
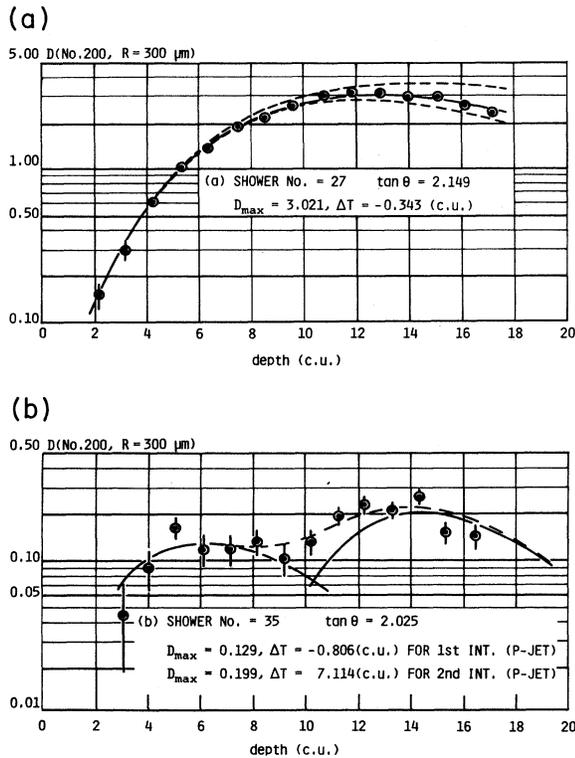

FIG. 12. Examples of autofitting of theoretical transition curves to experimental spot data with use of microcomputer. (a) is a case of the maximum energy event obtained in the present experiment, and (b) an example of successive interactions of a proton.
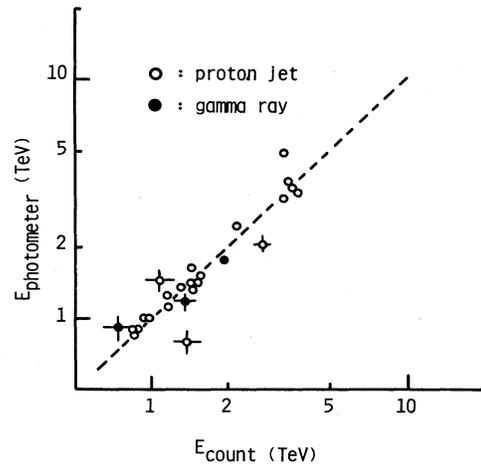

FIG. 13. Correlation between the energy obtained by the photometer and that by electron counting with use of nuclear emulsion plate.

D. Accuracy of the energy determination

Since the transition curves shown in Figs. 7 and 9 are average ones, the energy determined by fitting them to individual showers might be considerably different from the true one. As we have individual electron shower events in the process of the simulation calculation, we can transform them event by event into transition of spot darkness with use of Eq. (2), and determine each energy in the same way as described in Sec. III C.

Let us present the energy ratio $\sum E'_\gamma / \sum E_\gamma$ in Fig. 15, where $\sum E'_\gamma$ is the energy obtained by the above process, and $\sum E_\gamma$ the true one. In Fig. 16 we show the dispersion of the histogram against energy.

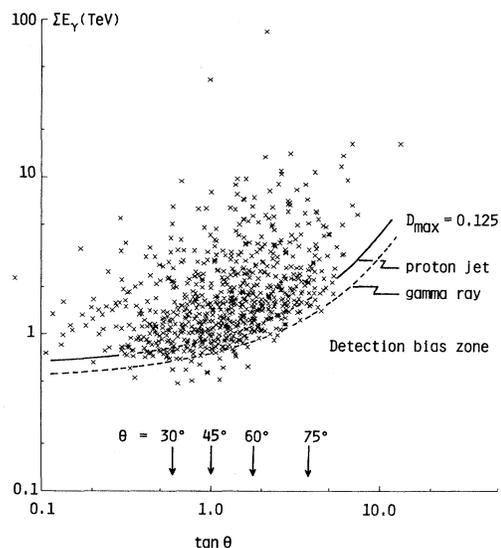These results are well within acceptable accuracy,

FIG. 14. Scatter plot of $\tan\theta$ vs $\sum E_\gamma$ for all showers detected in the present experiment. Curves of detection bias zone are determined from Fig. 10.
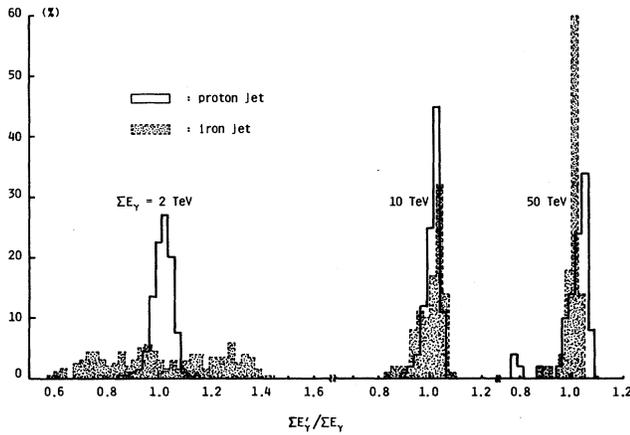
FIG. 15. Distribution of $\sum E'_\gamma / \sum E_\gamma$, where the numerator is the energy determined by the present auto-fitting system for each simulated event, and the denominator the true one.

though somewhat worse for iron jets with energies as low as 1–2 TeV. We discuss the conversion from $\sum E_\gamma$ to primary energy E_0 in Sec. IV B and Appendix E.

Looking at Fig. 16 carefully, one recognizes that σ increases gradually as the energy gets higher $\gtrsim 10$ TeV. This is because we limit the chamber thickness to 20 r.l. (~ 10 cm Pb) (r.l. is radiation length) in the simulation calculation, and events often emerge with shower-maximum depth beyond 20 r.l. at higher energies. One might think that the thickness 20 r.l. assumed here seems to be somewhat large in comparison with that of the present chamber, ~ 8 r.l. (see Sec. II A). This does not, however, result in a serious problem for the practical analysis, since the effective thickness becomes 12–16 r.l., taking account of the elongation of path length due to inclination effect ($\langle \cos\theta \rangle^{-1} = 1.5 \sim 2.0$). For instance, the zenith angle of the maximum shower energy ($\sum E_\gamma = 85.6$ TeV) detected by the present observation is 65° [see Fig. 12(a)], corresponding to the effective thickness of 18.6 r.l.
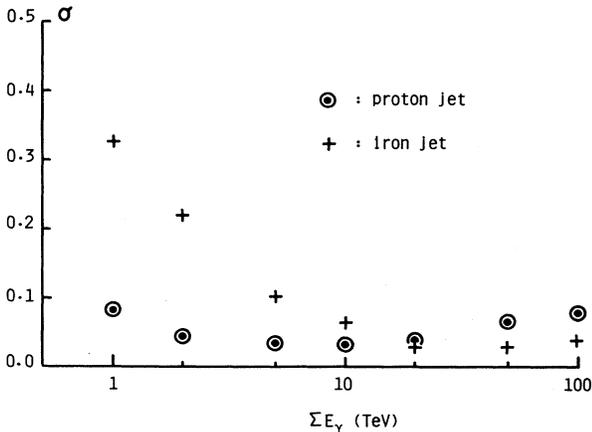
IV. CONVERSION TO ABSOLUTE INTENSITY OF PRIMARY

A. Detection efficiency

As the chamber structure for balloon-borne experiments is generally much more complicated than that for mountain experiments, it is difficult to estimate both the detection efficiency and the conversion factor to primary energy. In the present work, we obtain these quantities with the use of a numerical simulation.

Let us consider a chamber with area S ($=a \times b$) and height h, as drawn in Fig. 17. The effective area $S_{\rm eff}$ corresponding to the cutoff angle θ_c is given by

$$S_{\rm eff} = (a + 2h \tan\theta_c)(b + 2h \tan\theta_c)$$
$$= \left[1 + 2\frac{h}{a}\tan\theta_c\right]\left[1 + 2\frac{h}{b}\tan\theta_c\right]S . \quad (4)$$

Now, let $I(E_0, t)$ represent the vertical intensity of particle A with energy larger than E_0 at observation level t, then the total number of the particles falling on the effective area $S_{\rm eff}$ is given by

$$S_{\rm eff}(\theta_c)\Omega(t)TI(E_0, t) ,$$

where T and Ω are exposure time and effective solid angle, respectively. Ω depends on the kind of projectile A as well as observation level t, details of which are summarized in Appendix D.

In the simulation calculation, we first prepare N_0 projectiles with $E_0 \geq \sum E_\gamma$ on the effective area $S_{\rm eff}$, where the energies are sampled according to the distribution $E_0^{-\beta}$ (β is exponent of the integral energy spectrum), and second, perform random samplings for incident direction (θ, ϕ) according to the distribution functions Eqs. (D4) and (D5) (see Appendix D), and those for incident position (x, y). After setting these projectiles on $S_{\rm eff}$, we link them to the simulation program prepared for nuclear col-

FIG. 16. Correlation between the dispersion σ of $\sum E'_\gamma / \sum E_\gamma$ distribution and $\sum E_\gamma$.
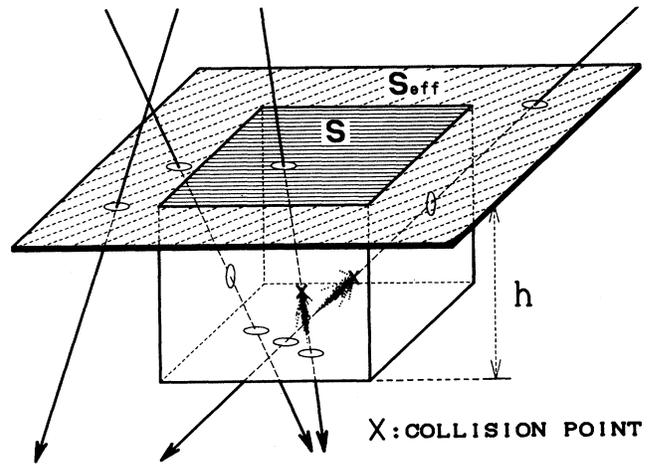

FIG. 17. Illustration of a collision of a cosmic-ray projectile with the chamber.

lisions inside the chamber, details of which are discussed in Appendix E.

Now, if we get N_{obs} events satisfying the detection criteria from these simulations (see Appendix E), (a) $\theta < \theta_c$, (b) observed energy released into γ's $\geq \sum E_\gamma$, and (c) $T_{\mathrm{path}} > T_{\mathrm{max}}$ ($= \langle T_{\mathrm{max}} \rangle + \Delta T$), the number of particles observed by the experiment, $J_{\mathrm{obs}}(\sum E_\gamma, t; \theta < \theta_c)$, is given by

$$J_{\mathrm{obs}} = \frac{N_{\mathrm{obs}}}{N_0} S_{\mathrm{eff}} \Omega T I \ , \tag{5}$$

leading to a result

$$I\left[\sum E_\gamma, t\right] = \frac{1}{\eta(\theta_c) S \Omega T} J_{\mathrm{obs}}\left[\sum E_\gamma, t; \theta < \theta_c\right] \ , \tag{6}$$

where

$$\eta(\theta_c) = \frac{N_{\mathrm{obs}}(\theta < \theta_c)}{N_0}\left[1 + 2\frac{h}{a}\tan\theta_c\right]\left[1 + 2\frac{h}{b}\tan\theta_c\right] \ . \tag{7}$$

Equation (7) is just the detection efficiency we need; that is, once getting N_{obs}/N_0 by simulation calculation, we can reduce the observed number of particles to the vertical intensity $I(\sum E_\gamma, t)$. In Table IV we summarize the detection efficiency η thus obtained for the present chamber structure, giving separately every projectile in the cases of $\theta_c = 60°$ and $75°$.

B. Conversion to primary energy spectrum

In order to get the primary energy E_0 from $\sum E_\gamma$, we need to know a conversion factor C_γ defined by

$$\sum E_\gamma = C_\gamma E_0 \ . \tag{8}$$

The factor C_γ is sensitive to the nuclear-interaction model. For instance, assuming the superposition model for nucleus-nucleus interaction, it is expressed as

$$C_\gamma = \frac{1}{A_p} \sum_{i=1}^{n_W} K_{\gamma i}$$

$$= w_A \langle K_\gamma \rangle \quad \text{with} \quad w_A = \frac{n_W}{A_p} \ , \tag{9}$$

where A_p is the mass number of projectile nucleus, n_W the number of participant nucleons (so called the "wounded" nucleons), and $K_{\gamma i}$ the inelasticity released into γ rays for nuclear interaction of the ith participant nucleon with one of those in target nucleus.

The average rate of wounded nucleons $\langle w \rangle_A$ is expressed, assuming the Glauber approximation,[21] as

$$\langle w \rangle_A \simeq \frac{\sigma_{N-B}}{\sigma_{A-B}} \ , \tag{10}$$

where σ_{N-B} and σ_{A-B} are the cross sections of nucleon versus nucleus B ($\equiv$ target) and nucleus A ($\equiv$ projectile) versus nucleus B, respectively.

Unfortunately C_γ fluctuates greatly, so that it is quite difficult to estimate E_0 from $\sum E_\gamma$ for *individual showers*. For practical purposes, however, we need to know only the relation between the $\sum E_\gamma$ spectrum $\tilde{I}(\sum E_\gamma)$ and the E_0 spectrum $I(E_0)$, that is, the *average scale shift* from the former to the latter. Assuming $I(E_0) \propto E_0^{-\beta}$, the former is easily expressed, with use of Eq. (8), as

$$\tilde{I}\left[\sum E_\gamma\right] = \int_{\sum E_\gamma}^\infty dE_0 \frac{dI(E_0)}{dE_0}$$

$$\times \int_0^1 f(C_\gamma)\delta\left[\sum E_\gamma - C_\gamma E_0\right]dC_\gamma$$

$$\propto \langle C_\gamma^\beta \rangle \left[\sum E_\gamma\right]^{-\beta}$$

$$\text{with} \quad \langle C_\gamma^\beta \rangle = \int_0^1 x^\beta f(x)dx \ , \tag{11}$$

leading to a result

$$I(E_0) = \tilde{I}\left[\sum E_\gamma / \langle \kappa_\gamma \rangle\right] \quad \text{with} \quad \langle \kappa_\gamma \rangle = \langle C_\gamma^\beta \rangle^{1/\beta} \ . \tag{12}$$

In Eq. (11) we introduced a distribution function $f(x)$, relating to the model of nuclear interaction. For instance, in the case of incident protons, it is well known that $\langle \kappa_\gamma \rangle$ is about $\sim \frac{1}{4}$ (Ref. 22), not affected *strongly* by the shape of $f(x)$.

The theoretical relation (12) is, however, not applicable straightforwardly for the practical analysis, since the

TABLE IV. Summary of conversion factor, detection efficiency, and attenuation length used in the present work, where the last one in the case of the γ ray (in parentheses) does not mean the attenuation in the usual sense (~ 100 g/cm^2), but is obtained by Λ_γ ($s = 1.8$) defined in Table X.

Particle	Conversion factor $\langle \kappa_\gamma \rangle$	Detection efficiency $\eta(\theta_c)$ $\theta_c = 60°$	Detection efficiency $\eta(\theta_c)$ $\theta_c = 75°$	Attenuation length in air (g/cm^2)
p, n	0.257	0.198	0.263	110.0
α	0.178	0.299	0.361	51.5
CNO	0.131	0.461	0.512	26.3
NeMgSi	0.108	0.532	0.572	21.0
Fe	0.098	0.651	0.678	14.8
γ	1.000	0.586	0.810	(178.2)
$\pi^\pm$	0.335	0.115	0.200	140.0

above-mentioned considerations do not take into account experimental conditions such as the error of the energy determination for $\sum E_\gamma$ (see Figs. 15 and 16), the limited thickness of the chamber, the successive nuclear interactions, and so on. In this paper, we obtain $\langle \kappa_\gamma \rangle$ (we call it the conversion factor again) by the simulation calculation as presented in Appendix E. The numerical values of $\langle \kappa_\gamma \rangle$ are shown in Table IV.

Though the value of $\langle \kappa_\gamma \rangle$ is quite reliable $(\Delta \langle \kappa_\gamma \rangle / \langle \kappa_\gamma \rangle \sim 10\%)$ for primary protons, for other species some ambiguities exist, coming mainly from the uncertainty of the wounded-nucleon rate $\langle w \rangle_A$ at our energy region. Recently, Fuki[23] performed extensive simulation calculations of nucleus-nucleus interaction on the basis of the multichain model,[24] and presented the conversion factor $\langle \kappa_\gamma \rangle$ for various kinds of projectile nucleus. We find the difference between the numerical values of $\langle \kappa_\gamma \rangle$ shown in Table IV and those given by Fuki is at most 10–20%.

In order to convert the primary flux $I(E_0,t)$, thus obtained at our observation level t, to that at the top of the atmosphere $I(E_0,t=0)$, we must assume the attenuation length Λ_A for the primary particle A, the numerical value of which is summarized in Table IV.

C. Contribution of cosmic-ray secondaries

Though most proton and α primaries arrive directly at the chamber at the level 32.8 g/cm^2, we have to take into account the contributions of nucleons and α's arising from the fragmentation of heavy primaries, and also those of $\pi^\pm$ from nuclear interactions. In this paper, we investigate their contributions in an analytical way, and compare it with those expected from the simulation of Ref. 9. We summarize analytical expressions for the flux of various components in Appendix B, and give the diffusion of fragment-nucleons coming from α in Appendix C.

The observed number of "proton" jets, including secondaries such as fragment nucleons and $\pi^\pm$, is expressed as

$$J_{\text{obs},p} = J_p + \sum_{A \geq \alpha} J_{A \to N} + \sum_{A \geq p} J_{A \to \pi^\pm} , \qquad (13)$$

each related to the vertical intensity by

$$J_p = \eta_p S \Omega_p T I_p , \qquad (14a)$$

$$J_{A \to a} = \eta_{A \to a} S \Omega_{A \to a} T I_{A \to a} \quad (a = N, \pi^\pm) ; \qquad (14b)$$

here, I_p denotes the vertical intensity of both primary protons and charge-exchanged neutrons. Explicit forms of $I_{A \to N}, I_{A \to \pi^\pm}$ are summarized in Appendix B. So, we have the relation

$$\frac{J_{\text{obs},p}}{J_p} = 1 + \epsilon_N + \epsilon_{\pi^\pm} , \qquad (15)$$

$$\epsilon_a = \sum_{A \geq \alpha,p} \frac{\eta_{A \to a}}{\eta_p} \frac{\Omega_{A \to a}}{\Omega_p} \frac{I_{A \to a}}{I_p} \quad (a = N, \pi^\pm) . \qquad (16)$$

ϵ_N and $\epsilon_{\pi^\pm}$ denote the contamination rates we need for fragment nucleons and charged pions, respectively, against proton jets.

In Fig. 18 we demonstrate the altitude variations of $\epsilon_N, \epsilon_{\pi^\pm}$ and their sum $\epsilon_N + \epsilon_{\pi^\pm}$ (heavy solid curve), together with those obtained by simulations, where we assumed exponents of integral energy spectra to be 1.8 for protons and α's, 1.7 for CNO and NeMgSi, and 1.5 for iron, and we set the primary energy at 10 TeV/nucleon.

In Table V, we summarize ϵ_N and $\epsilon_{\pi^\pm}$ at our observation level, giving contributions from each mode separately, and found the total contamination rate is as small as $\sim 22\%$.

Similarly as in the case of Eq. (15), we can express

TABLE V. Explicit numerical values of ϵ_N and $\epsilon_{\pi^\pm}$ at our observation level. The two values for $\pi^\pm$ for the analytical case correspond to the choice of inelasticity as 0.5–0.6.

	Process	Analytical	Simulation
p	$\to p, n$ (survival)	1	1
p	$\to \pi^\pm$	3.92–4.72%	4.68%
α	$\to p, n$	8.01%	9.24%
	$\to \pi^\pm$	1.01–1.21%	1.00%
CNO	$\to p, n$	2.40%	1.74%
	$\to \pi^\pm$	0.13–0.16%	0.11%
NeMgSi	$\to p, n$	1.98%	1.80%
	$\to \pi^\pm$	0.09–0.11%	0.18%
Fe	$\to p, n$	4.41%	2.65%
	$\to \pi^\pm$	0.19–0.29%	0.29%
Total except $p \to p, n$		22.14–23.23%	21.69%
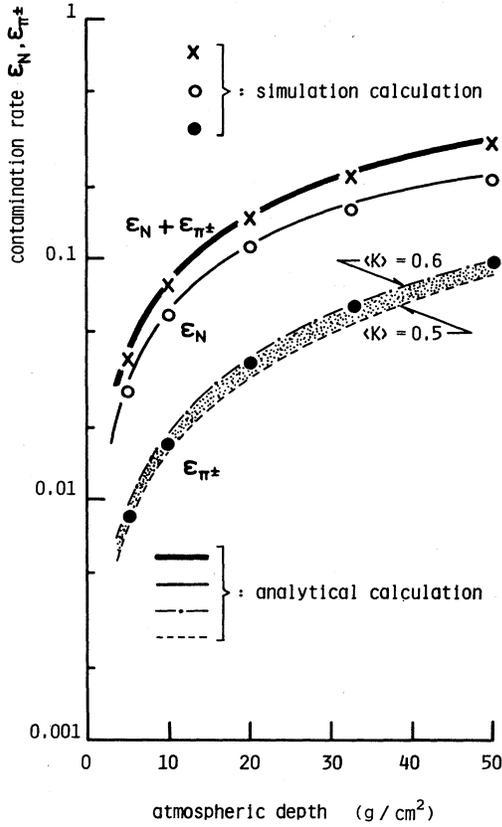
FIG. 18. Altitude variation of ϵ_N and $\epsilon_{\pi\pm}$. $\langle K \rangle$ denotes the average inelasticity of nucleon vs air-nucleus interactions.

FIG. 19. Altitude variation of ϵ_α.

$$\frac{J_{\mathrm{obs},\alpha}}{J_\alpha} = 1 + \epsilon_\alpha , \qquad (17)$$

$$\epsilon_\alpha = \sum_{A>\alpha} \frac{\eta_{A\to\alpha}}{\eta_\alpha} \frac{\Omega_{A\to\alpha}}{\Omega_\alpha} \frac{I_{A\to\alpha}}{I_\alpha} , \qquad (18)$$

where ϵ_α denotes the contamination rate of α's coming from the fragment of heavy primaries ($\gtrsim$ CNO) against surviving *primary* α's, and the explicit form of $I_{A\to\alpha}$ is presented in Appendixes B and C. In Fig. 19 we show the altitude variation of ϵ_α, together with the result of the simulation. In Table VI we show ϵ_α at our observation level, giving contributions from each mode separately, indicating that the contamination rate of α's for primary α's is as small as $\sim 7\%$.

D. Zenith-angle distribution

In the process of the simulation presented in Sec. IV A, we sampled the zenith angle of the projectile at the top of the chamber, according to Eqs. (D4) and (D5) in Appendix D. The zenith-angle distribution actually detected in the chamber is of course different from that at the top of the chamber, because of the penetration effect, triggering bias affected by path length and so on, all of which depend on the chamber structure and the detection conditions.

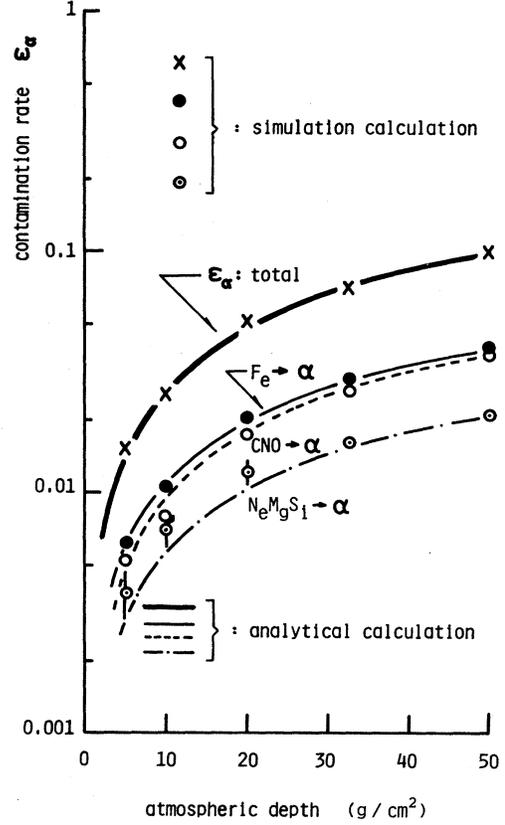In Fig. 20 we present the zenith-angle distribution ob-

tained by the present observation in the cases of γ, proton, and α projectiles with energy $\sum E_\gamma \geq 2$ TeV, where those obtained by the simulation are also shown. One finds that both results are nearly consistent with each other, although a slight deviation is found at $\sec\theta = 1.0$–1.3 for γ rays.

TABLE VI. Explicit numerical values ϵ_α at our observation level.

	Process	Analytical	Simulation
α	$\to\alpha$ (survival)	1	1
CNO	$\to\alpha$	2.52%	
	$\to A'\to\alpha$	0.22%	
	Subtotal	2.74%	2.59%
NeMgSi	$\to\alpha$	1.21%	
	$\to A'\to\alpha$	0.36%	
	Subtotal	1.57%	1.64%
Fe	$\to\alpha$	2.23%	
	$\to A'\to\alpha$	0.71%	
	Subtotal	2.95%	2.94%
Total except $\alpha\to\alpha$		7.26%	7.17%
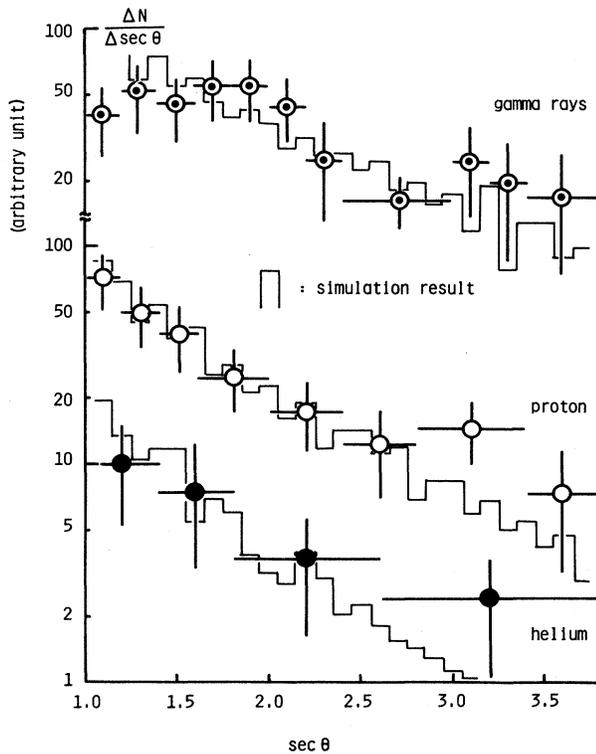
FIG. 20. Zenith-angle distributions for γ, proton, and α obtained by the present experiment.

V. EXPERIMENTAL RESULTS

A. Primary composition and energy spectrum

1. Protons

After subtracting the background of 22% from the observed number of "protons" on the basis of the discussions in Sec. IV C, we can obtain the vertical intensity of protons $I(\sum E_\gamma, t)$ (including charge-exchanged neutrons), as defined by Eq. (6), at our observation level $t = 32.8$ g/cm^2. Now assuming $\Lambda_p = 110$ g/cm^2 (attenuation length in air) and $\langle \kappa_\gamma \rangle = 0.257$ (conversion factor) (see Table IV), we can convert this to the intensity of primary protons, $I(E_0)$, at top of the atmosphere, the result of which is shown, in the differential form, in Fig. 21, where we present also the intensity of other primaries, α, CNO, . . . , obtained by the present experiment.

In Fig. 22 we present the proton spectrum, in integral form, together with other data. We found that our data agree well with JACEE data[3] in the region $E_0 \gtrsim 5$ TeV, and disagree significantly with those obtained by Grigorov et al.[1] and Abulova et al.[2] We guess that this is probably due to the absolute energy calibration and/or the calculation of detection efficiency. Unfortunately, we

FIG. 21. Differential spectrum of various cosmic-ray primaries obtained by the present experiment. Straight lines are those expected from Eqs. (19)–(21).
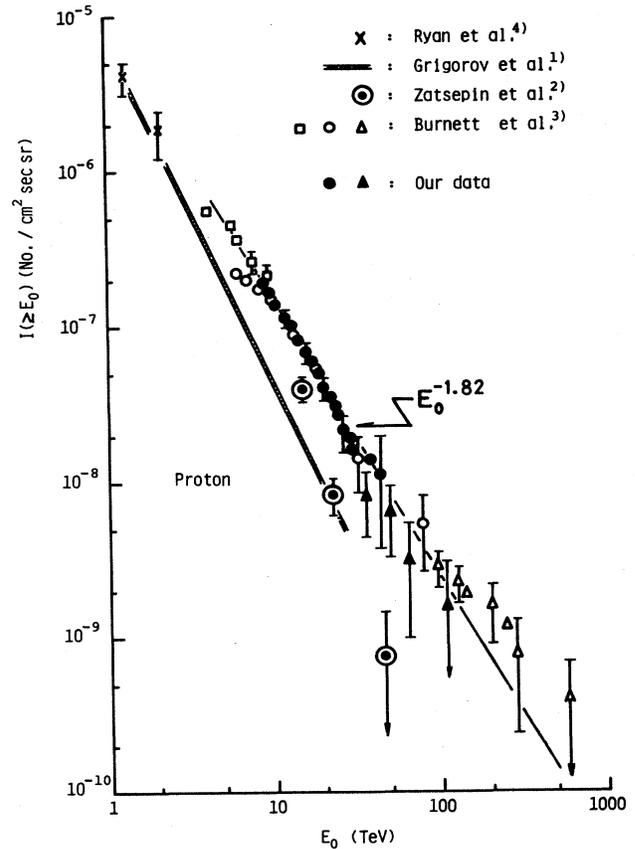

FIG. 22. Integral intensity of primary protons. A closed circle is obtained directly by the present experiment, while a closed triangle is obtained quasidirectly from the γ-bundle flux.

cannot discuss more quantatively the numerical procedures used by each group, since these are not described explicitly in their papers. At energies above 50 TeV, the JACEE flux seems to be somewhat larger than that extrapolated from our data.

We obtain the absolute intensity of protons in an integral form as

$$I_p(E_0) = I_p^{(0)} E_0^{-1.82 \pm 0.13} \quad (E_0 \text{ in TeV}) , \tag{19a}$$

with

$$I_p^{(0)} = 1.02 \times 10^{-5} \text{ (cm}^2 \text{ sec sr)}^{-1} , \tag{19b}$$

for $E_0 \gtrsim 5$ TeV.

In Figs. 21 and 22 we present also the data obtained from the energy-flow spectrum of the γ-ray bundles (closed triangles), which will be discussed later.

2. α particles

Subtracting the contamination of 7% from the observed number of α's, as discussed in Sec. IV C, and assuming $\Lambda_\alpha = 51.5$ g/cm^2 (attenuation length) and $\langle \kappa_\gamma \rangle = 0.178$ (see Table IV), we obtain the intensity of primary α's at the top of the atmosphere, which is shown, in the differential form, in Fig. 21 (open circle).

In Fig. 23 we show the integral intensity of primary α's together with other data. One finds again a clear discrepancy with the data by Grigorov *et al.*, but our data are compatible with those of JACEE group. The data by Abulova *et al.* seem to give a lower intensity in the region $\lesssim 10$ TeV/nucleon.

We obtain the intensity of α at the top of the atmosphere:

$$I_\alpha(E_0) = I_\alpha^{(0)} E_0^{-1.75 \pm 0.15} \quad (E_0 \text{ in TeV/nucleon}) , \tag{20a}$$

with

$$I_\alpha^{(0)} = 6.50 \times 10^{-7} \text{ (cm}^2 \text{ sec sr)}^{-1} , \tag{20b}$$

for $E_0 \gtrsim 3$ TeV/nucleon.

3. Heavy primaries (≥ CNO)

Though the statistics of heavy primaries observed are not sufficient in the present exposure, we show differential intensities of these in Fig. 21, and give integral spectra, together with other data, in Figs. 24 (CNO and NeMgSi groups) and 25 (Fe group).

The conversion factor and the detection efficiency are given in Table IV. In Figs. 24 and 25 we put a width of 2σ for energy as given in Fig. 16.

Referring to other data as well as ours, we express these intensities in an integral form as

$$I_A(E_0) = I_A^{(0)} E_0^{-\beta_A} \quad (E_0 \text{ in TeV/nucleon}) , \tag{21}$$

and we give explicit numerical values of $I_A^{(0)}$ and β_A for the three groups, CNO, NeMgSi, and Fe, in Table VII, where we present also the energy range valid for such parametrizations.
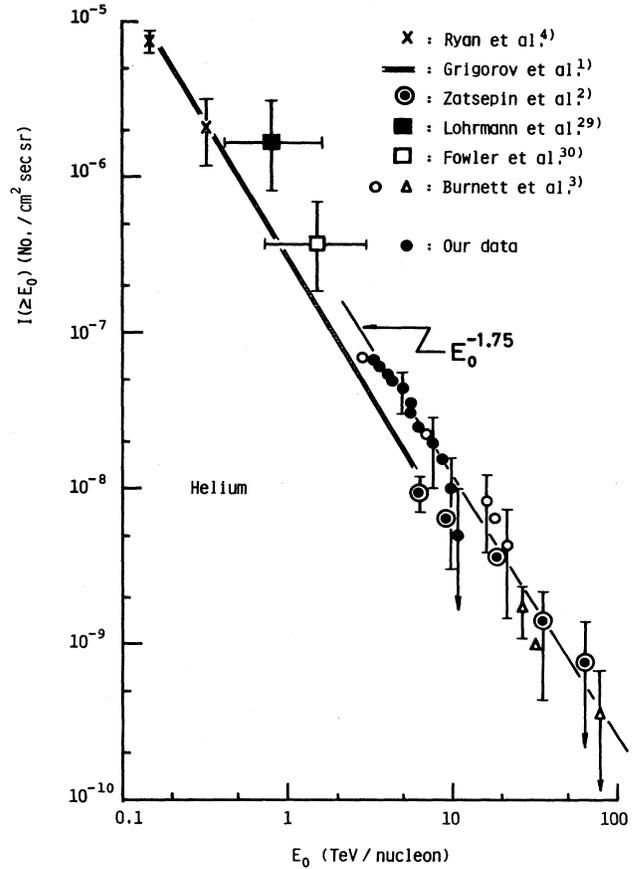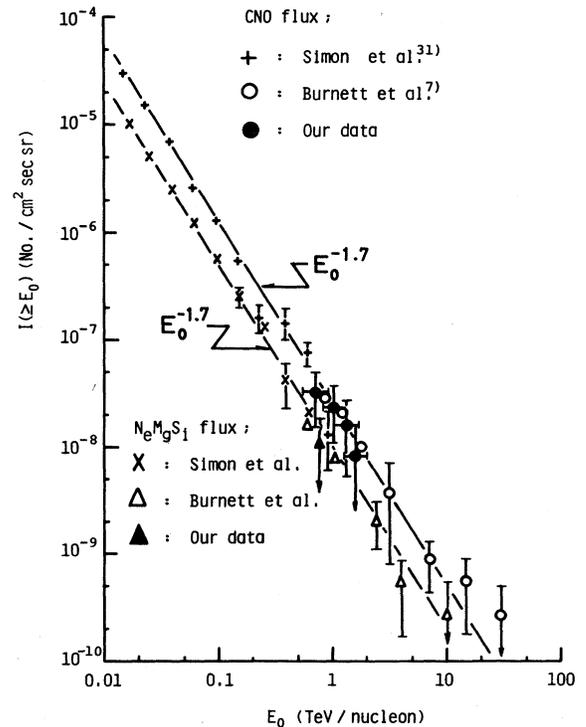

FIG. 23. Integral intensity of primary α.

FIG. 24. Integral intensity of CNO, NeMgSi groups.

TABLE VII. Summary of numerical values of $I_A^{(0)}$ and β_A defined in Eq. (21). Energy range valid for these parametrizations is also shown.

A	$I_A^{(0)}$ (cm^2 sec sr)$^{-1}$	β_A	Energy range (eV/nucleon)
CNO	2.55×10^{-8}	1.70 ± 0.10	$10^{10} - 10^{13}$
NeMgSi	9.70×10^{-9}	1.70 ± 0.10	$10^{10} - 10^{13}$
Fe	3.70×10^{-9}	1.50 ± 0.20	$\gtrsim 10^{11}$

B. Atmospheric secondary γ rays and primary composition

1. Comparison with other data

In Fig. 26 we show the vertical intensity of atmospheric secondary γ rays in the differential form at our observation level, where electrons are also included, since it is sometimes difficult to distinguish experimentally between the two, though the contribution is small at the stratospheric level. Of course, the contribution of primary electrons to the atmospheric electrons (and γ's) is negligibly small in the energy region $\gtrsim 10^{12}$ eV at our observation level, since the differential power index of the former is known to be 3.3–3.6 (Ref. 25), much steeper than that of cosmic-ray nuclei (~ 2.8), and since most of the electrons are affected by the cascade degradation in the overlying atmosphere.

We plot the data obtained by Nishimura et al.[25] (observation level $= 9.5$ g/cm^2) together with ours in Fig. 26 after normalizing to our level 32.8 g/cm^2. Of course, it is not so meaningful to compare the above two if the normalization procedure depends strongly on the model of nuclear interactions. This can be, however, performed model independently as follows.

The γ-ray flux at level t is generally expressed as (see Appendix B)

$$\langle n_\gamma \rangle_p \frac{t}{\lambda_p} \left[1 + \frac{1}{2} \frac{t}{\Lambda_{p\gamma}(\beta_p)} + \cdots \right] I_p(E,t) , \qquad (22)$$

where the terms correspond to production rate of γ's per collision, collision times of primary particle, correction term, and intensity of primary particle at level t.

As shown in Appendix B, for example, putting $\Lambda_p = 110$ g/cm^2 and $\beta_p = 1.8$, we get $\Lambda_{p\gamma} = 215$ g/cm^2;
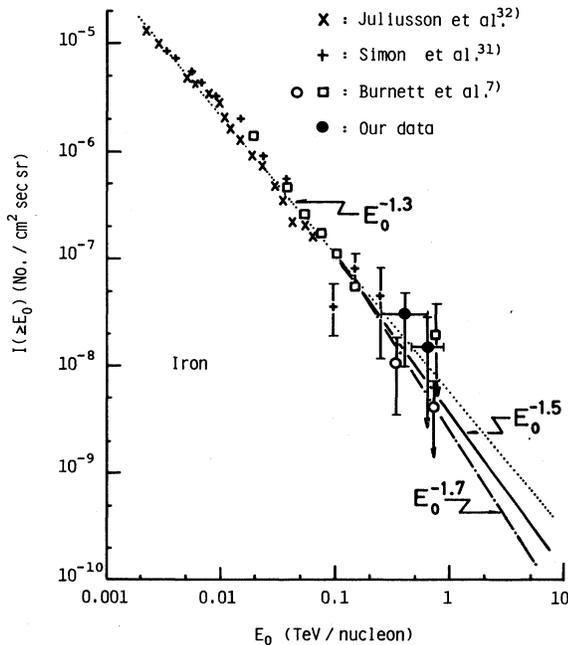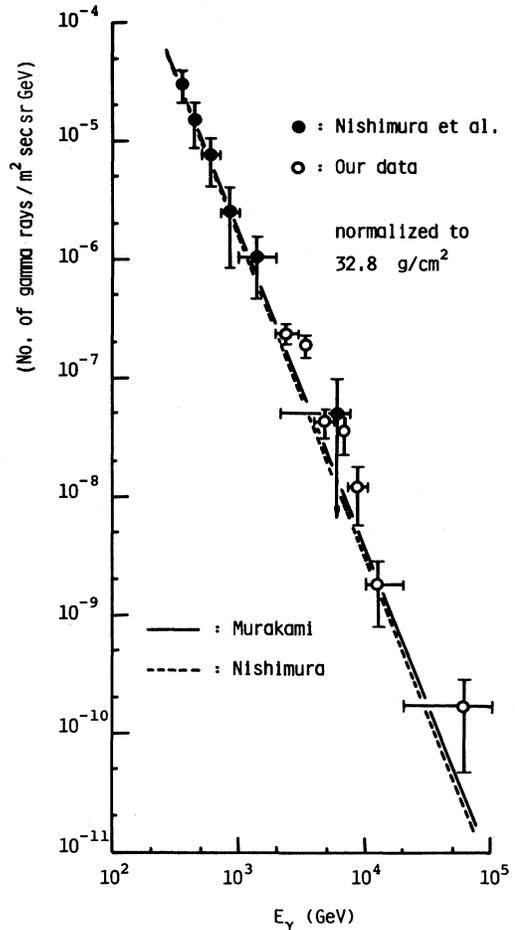

FIG. 25. Integral intensity of Fe group.

FIG. 26. Differential vertical flux of γ at our observation level 32.8 g/cm^2. Data of Nishimura et al. (observation level $= 9.5$ g/cm^2) are normalized to our level.

i.e., the correction term is of the magnitude $\sim 7\%$ at our level. Now, the relative flux ν between two levels t_1 and t_2 $(t_1 < t_2)$ is expressed by

$$\nu = \frac{I_\gamma(t_2)}{I_\gamma(t_1)}$$

$$= \frac{t_2}{t_1}\left[1 + \frac{1}{2}\frac{\Delta t}{\Lambda_{p\gamma}} + \cdots\right]e^{-\Delta t/\Lambda_p}$$

with

$$\Delta t = t_2 - t_1 \; ; \tag{23}$$

that is, the model-dependent term $\langle n_\gamma\rangle_p$ is canceled out and only the spectrum index β_p and attenuation length Λ_p of the primary particle is related to ν. One should further remark that since the above two β_p and Λ_p appear in the forms of second-order corrections $\Delta t/\Lambda_p$ and $\Delta t/\Lambda_{p\gamma}(\beta_p)$, the ambiguity of the choice of the numerical values presents no problems, and only the ratio of the two observation levels t_1 and t_2 is the principal term. For instance, putting $\Lambda_p = 110$ g/cm^2, $\beta_p = 1.8$, $t_1 = 9.5$ g/cm^2, and $t_2 = 32.8$ g/cm^2, the normalization factor ν is 2.95, that is, multiplying the data of Nishimura et al. by 2.95 gives the γ-ray intensity at our level.

As seen in Fig. 26, our data overlap with those of Nishimura et al., and seem to be approximately consistent with the extrapolation from the low-energy region. We draw two straight lines expected from the calculations of Murakami et al.[26] and Nishimura et al.,[25] the former (solid line) derived from the proton spectrum and the latter (dashed line) from the muon spectrum. Looking carefully, we find that the present result seems to be somewhat overabundant in comparison with these predictions in the low-energy region. A possible interpretation of the γ-ray enhancement in the energy region 2–80 TeV is discussed in the following section.

2. γ-ray spectrum and primary composition

As shown in Fig. 26, the γ-ray energies we observed cover 2–80 TeV. These γ rays must have been produced by primaries with much higher energies. We performed a simulation calculation to determine the mean energy of a cosmic-ray primary corresponding to each γ ray observed at the depth of 32.8 g/cm^2, the result of which is shown in Fig. 27, where $\langle E_0\rangle$ denotes the geometric mean for primary energies in each bin.

We found the primary energy to be 8 times larger on average than the observed γ-ray energy, indicating that the data of Fig. 26 reflect the energy spectrum of primaries in the region 10–100 TeV/nucleon. In turn, it tells us that we can deduce the primary spectrum at much higher energies from the investigation of the γ-ray intensity.

First, we estimate the γ-ray flux coming from primary protons alone. Since we have the intensity of protons in Eq. (19), reliable up to ~ 100 TeV, we can get the γ-ray flux with use of the formula in Appendix B as
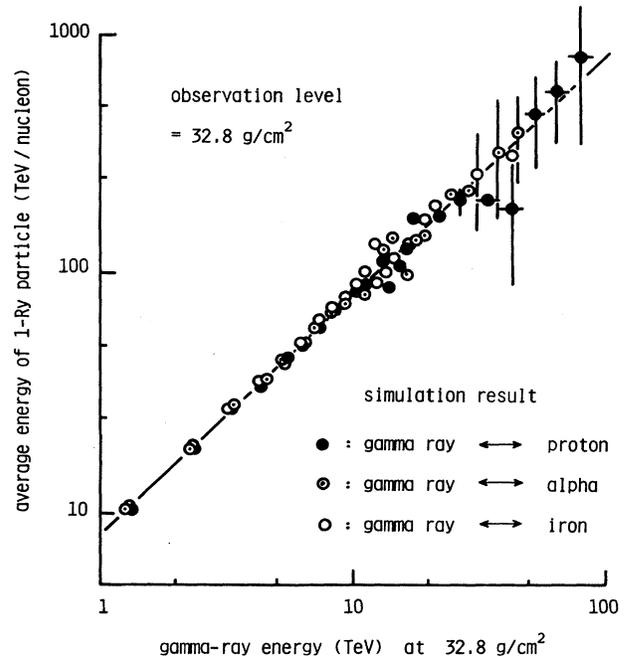

FIG. 27. Relationship between γ-ray energy observed at 32.8 g/cm^2 and the average primary energy (per nucleon) producing them, where primaries are assumed to be proton (closed circle), α (sun symbol), and iron (open circle).
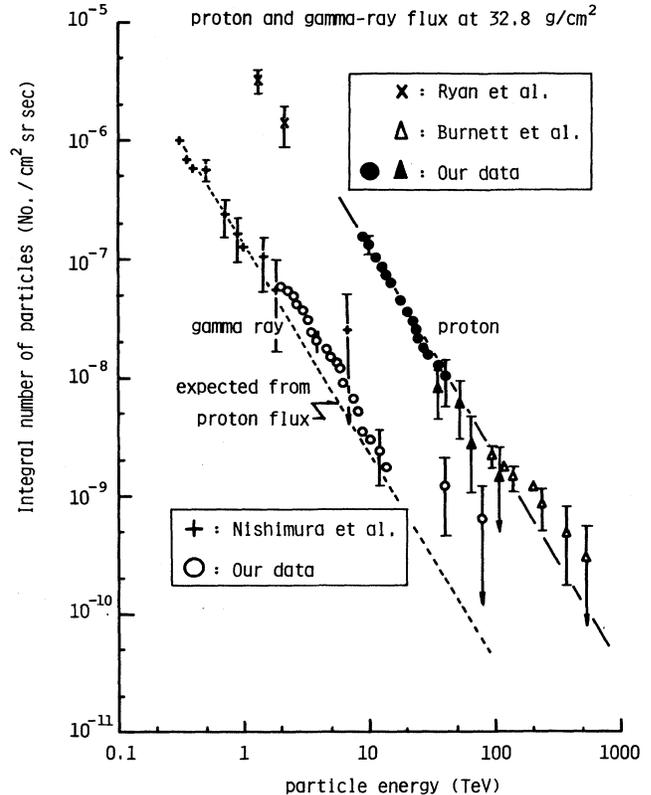

FIG. 28. Integral vertical flux of protons and γ at our observation level. The dashed line is the γ-ray flux expected from the proton flux (solid straight line).
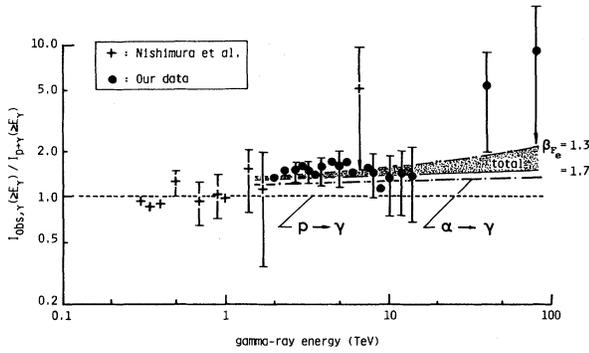
FIG. 29. Integral vertical flux of γ's normalized by the expected flux $I_{p \to \gamma}$ of proton-originated γ's. Upper and lower limit for dotted area correspond to the indices of energy spectrum 1.3 and 1.7, respectively.

$$I_{p \to \gamma}(E_\gamma, t = 32.8 \text{ g/cm}^2)$$

$$= I_{p \to \gamma}^{(0)} E_\gamma^{-1.82} \quad (E_\gamma \text{ in TeV}) , \quad (24a)$$

with

$$I_{p \to \gamma}^{(0)} = 1.41 \times 10^{-7} \text{ (cm}^2 \text{ sec sr)}^{-1} . \quad (24b)$$

In Fig. 28 we show both integral intensities together, proton and γ, at our observation level, where the straight lines expected from Eqs. (19) (solid line) and (24) (dashed line) are also drawn. One finds that the measured spectrum of γ rays is significantly larger than expected. In order to make the situation clearer, we divide the experimental γ-ray flux by the expected flux from Eq. (24), and investigate the contributions of γ's coming from primaries other than protons. This is shown in Fig. 29.

Figure 29 shows that even if we take the contribution of γ's arising from α's into account [dashed-dotted line expected from Eq. (20)], our data still give a considerable excess. This indicates that γ's generated by heavy primaries ($\gtrsim$ CNO) become significant in the energy region $\gtrsim$ several TeV. As we presented in Sec. V A 3, the most ambiguous data among the heavy primaries in the energy region of concern are those of iron, so that we consider three cases of spectral indices, 1.3, 1.5, and 1.7, as shown in Fig. 25, for the iron component, while we use numerical values given in Table VII for the other two components: CNO and NeMgSi groups. The result is shown in Fig. 29 as a dotted area, telling us that the γ-ray excess might originate in the iron dominance at higher energies.

3. γ-ray bundles and primary proton spectrum

The definition of a γ-ray bundle here is $N_\gamma \geq 2$, where each constituent γ has energy ≥ 1 TeV, and where the incident directions coincide with each other within experimental error, less than $\Delta\theta \lesssim 20'$ and $\Delta\phi \lesssim 50'$ with the use of the nuclear emulsion plate. The chance coincidence of background parallel γ's is extremely small with these selection criteria. In the present observation, we obtained eight events satisfying the above conditions, among which five events have energy $\sum E_\gamma \geq 9$ TeV.

Now, which primary is the most effective for these bundles? We expect that most of the heavy components such as iron break up near the top of the atmosphere, well above our observation level of 32.8 g/cm^2. The lateral spread of the bundle would then be extremely large when it arrives at our detector, far larger than the chamber area (50 $\times$ 80 cm^2), so that few bundles coming from heavy components are observed in the present experiment. In fact, applying the simulation calculation for γ-ray bundles taking into account the detection efficiency as well as the selection criteria mentioned above, we obtain the relative detection rates of γ bundles for each primary as

$$p:\alpha:\text{CNO}:\text{NeMgSi}:\text{Fe} = 1:0.21:0.036:0.023:0.045 \quad (25)$$

for $\sum E_\gamma = 9-50$ TeV. Of course, this depends on the observed energy range $\sum E_\gamma$, since the spectral indices assumed here are different among the above five primary groups [see Eqs. (19) and (20), and also Table VII], and the rate of γ bundles coming from irons will increase with higher-energy region, if the spectral index of iron in such region remains as hard as in the lower-energy region $\beta \sim 1.5$.

Next, we convert the energy flow $\sum E_\gamma$ of the bundle to the primary energy $E_0 = \sum E_\gamma / \langle \kappa_\gamma \rangle$. In Fig. 30 we show the distribution of κ_γ, obtained by the simulation, where the primary is assumed to be a proton. One sees that both the shape of the distribution and the average value (=0.272; geometric average) are quite similar to those in the case of a local nuclear interaction.
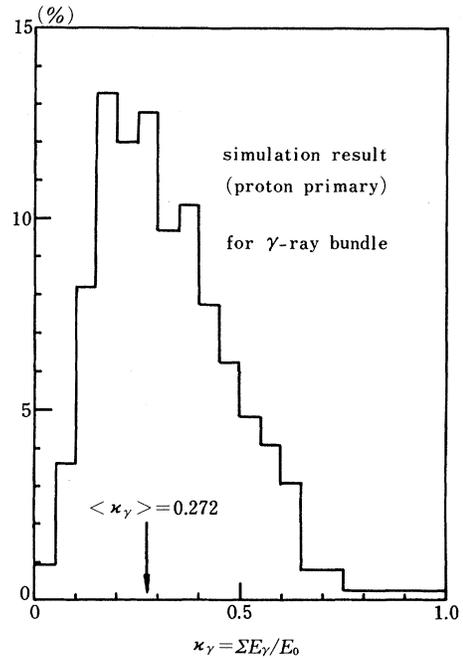
Similarly as in the case of Eq. (6), we have a relation

FIG. 30. Distribution of the ratio $\sum E_\gamma / E_0$, where $\sum E_\gamma$ denotes the energy of the γ-ray bundle and E_0 the energy of the primary proton producing it.

$$I\left[E_0 = \sum E_\gamma / \langle \kappa_\gamma \rangle, \quad t = 0\right]$$

$$= \frac{1}{\eta^* S \Omega T} J_{\text{obs}} \left[\sum E_\gamma, \quad t = 32.8 \text{ g/cm}^2\right] \quad (26)$$

with $\eta^* = 0.414$.

The detection efficiency η^* defined here is somewhat different from the value for the case of single γ's given in Table IV, since we have to take into account the absorption effect in the atmosphere due to the spread of bundles mentioned above.

After subtracting the 31.4% contribution coming from primaries other than protons [see Eq. (25)], we obtain the spectrum as shown in Figs. 21 and 22 (closed triangles). One finds that the proton spectrum seems to continue up to ~ 100 TeV with an index of -1.8 to -1.9, though the statistics are poor and these are not "purely direct" data.

VI. DISCUSSIONS

We observed many atmospheric secondary γ rays (and γ bundles) as well as cosmic-ray primaries (p, α, CNO, ...) directly in our chamber. As is well known, high-energy atmospheric γ rays ($\gtrsim *$TeV) observed at mountain level ($\gtrsim 500$ g/cm^2) originate overwhelmingly from proton primaries, and those from heavier nuclei are obscured, even if the latter primaries (α, CNO, ...) are more abundant than the formers.[5] This is because, first the energy of secondary γ's produced by heavy-primary interaction with an air nucleus is, on average, much lower than that by proton interaction for the same primary energy (/nucleus), and second, the atmosphere ab-

sorbs most of the γ rays, produced by heavy primaries, during the passage from the interaction place (mostly very near the top of atmosphere) to the mountain level.

We expect, on the other hand, at our observation level of 32.8 g/cm^2, that because of the rare atmosphere, γ rays originating from cosmic-ray primaries other than protons are also significant. In particular, those arising from iron might become more dominant than those from protons, provided that the index of the iron energy spectrum remains as flat as in the lower-energy region up to the region we are concerned with, say ~ 100 TeV/nucleus. In fact, as shown in Sec. V B 2, we found that the observed γ rays are much more abundant than those expected from protons and α's alone, indicating a flat energy spectrum for the iron component with an index ~ 1.5 still in the region ~ 100 TeV/nucleus. These features are nearly compatible with the most recent result, ~ 1.55 (Ref. 8), obtained by a space-borne experiment. We must, however, keep in mind that we observed no hadron bundles (p, n, α) in the present experiment, so that we cannot extrapolate the iron spectrum so excessively, but have to set some upper limit as discussed later.

The speculation mentioned above is of course based on the assumption that no anomaly of the nuclear interaction occurs at the energy region we are concerned with. That is, if secondary γ's (mostly originating from $\pi^0 \to 2\gamma$) are produced more excessively in the forward (pseudo)rapidity region than $\pi^\pm$, we do not need to introduce such a flat spectrum of the iron component as mentioned above. Recent results of the Fermilab collider experiment by the CDF group,[27] though preliminary, show none of such excess, while the JACEE group[28] report
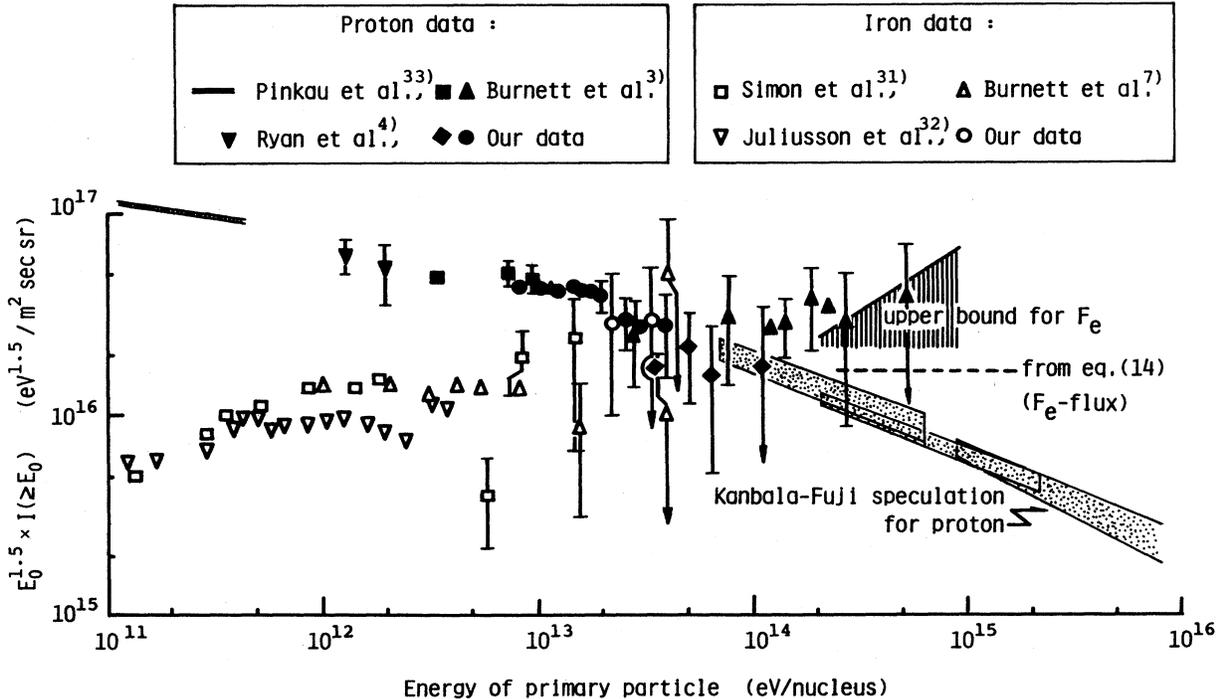

FIG. 31. Primary spectra for protons (solid symbols) and iron (open symbols) obtained by many authors, where the vertical axis is multiplied by $E_0^{1.5}$.

such a signal. So, one should mind that the present speculation depends on the feature of nuclear interaction, particularly in the diffractive region.

Now, let us summarize the energy spectra of protons and iron, multiplied by $E_0^{1.5}$ to emphasize their difference, in Fig. 31 together with the data of other authors.

As seen in Fig. 31, the intensities of proton and iron seem to cross each other somewhere between 10^{14} and 10^{15} eV/nucleus, though the latter data fluctuate widely in the region $\gtrsim 10$ TeV/nucleus. It is remarkable that the enhancement of the γ-ray intensity is well explained by such a flat iron spectrum with index ~ 1.5. In Fig. 31 we draw the dotted line expected from the γ-ray spectrum in the region 2–20 TeV, corresponding approximately to the energy of iron primary 10–100 TeV/nucleus.

We have to, however, set upper limit for the iron spectrum, since no hadron bundles, most of which would be produced by iron, are detected in the present observation. On the basis of simulations, taking into account the detection efficiency, we obtained its limit as shown in Fig. 31 (zone with oblique lines). So, it is quite critical to detect hadron-bundle, particularly accompanying α's, for the intensity of iron in the region ~ 1000 TeV/nucleus.

In Fig. 31 we present also the proton spectrum deduced indirectly from emulsion-chamber experiment[5] at mountain level, overlapping with our data in the region 50–100 TeV. Looking on the whole from the lower-energy region ~ 0.1 TeV, we found the index seem to change gradually from $-1.6-\,-2.0$.

In a forthcoming paper, we will report our results in connection with EAS data as well as some speculation on the source spectrum of cosmic rays.

ACKNOWLEDGMENT

APPENDIX A: PRACTICAL PROCEDURE OF THE ENERGY DETERMINATION OF CASCADE SHOWER

Here we summarize the procedure to determine the cascade energy with use of the spot darkness recorded on x-ray film (Fuji No. 200 type). In Fig. 32 we illustrate the flow chart of the energy determination process, and explain essential points below. The energy determination from the electron counting with use of the nuclear emulsion plate is essentially the same as Fig. 32 after replacing the photodensitometer by the microscope.

Step 1, registration of chamber structure. We register each material thickness sequentially on disk from the top of chamber to the bottom, including the various kinds of materials such as heavy absorbers (lead here), sensitive
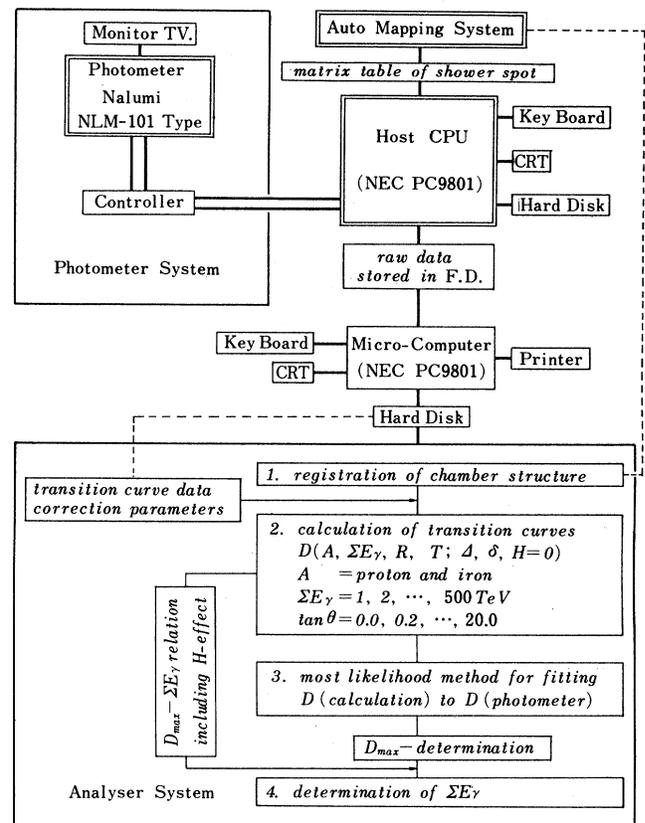

FIG. 32. Flow chart of our energy determination system with use of photodensitometer.

materials (x-ray film, nuclear emulsion plate, . . .), acrylic producer, spacer, etc., whose material constants, mass number, density, radiation length, and so on, are all registered beforehand.

Step 2, calculation of transition curves. We calculate transition curves for the calorimeter part registered in step 1, taking into account the heterogeneous effect, details of which are presented in Ref. 10. Here we always calculate three kinds of transition curves, first initiating from a γ ray (e pair), the second from a proton jet, and the third from an iron jet, in the energy range $\sum E_\gamma = 1$–500 TeV, taking into account the effect of zenith angle of incidence.

In this step, we calculate also the relation between $D_{\max}$ (maximum of transition curve) and $\sum E_\gamma$, which we use to determine the final energy.

Since experimentally the interaction position occurred in target layer (or often in calorimeter part too) differ from event to event, we set $H = 0$ (H is interaction height from the top of calorimeter part), in this step, and take into account the effect of $H \neq 0$ in step 4.

Step 3, theoretical curve fit to experimental data. We fit the theoretical transition curves obtained in the step 2 to experimental data with use of the least-squares method, details of which are summarized in Ref. 34. Thus we obtain the maximum peak of transition curve $D_{\max}$.

TABLE VIII. Explicit expressions of the production rate $\langle n_a \rangle_A$ for various combinations of observed particle a and its primary A. Here, $\langle w \rangle_p = 1$ and A is the mass number corresponding to primary A.

A	a	$\langle n_a \rangle_A$
$A(\geq p)$	$\pi^{\pm}$	$\frac{2}{3}A\langle w \rangle_A \Phi(\beta_A)$
	γ	$\frac{1}{\beta_A + 1}\langle n_{\pi^{\pm}} \rangle_A$
$A(\geq \alpha)$	p,n	$A\left[1 - \dfrac{\langle w \rangle_A \lambda_p}{\Lambda_p}\right]$
$A(\geq X)$	$X(\geq \alpha)$	P_{AX}

In the step 3, we prepare the maximum spot darkness $D_{\max}$, so that we can obtain uniquely the energy $\sum E_\gamma$ from Fig. 10 in text. The energy thus obtained is, however, not final, since we have to further take into account the effects of the interaction height H (called H effect) and the mass number of incidence A.

For the H effect, it is necessary to perform the following replacement:

$$D_{\max} \rightarrow D_{\max}/[q_3(H)]^\mu|_{t=t_{\max}} , \tag{A1}$$

with

$$q_3(H) = \frac{1 - e^{-U_3(H)}}{U_3(H)} \quad \text{and} \quad U_3(H) = \alpha_3 H^{\beta_3} , \tag{A2}$$

where the explicit numerical values of correction parameters α_3, β_3, and μ are given in Ref. 10, and they are of course stored on disk in our analyzer system.

On the mass-number effect, we apply the "proportional allotment method" as shown in Sec. III A in text.

APPENDIX B: FLUX OF SECONDARY COSMIC RAYS AT STRATOSPHERIC LEVEL

In order to get the flux of cosmic-ray secondaries, we often use the quantity

$$\Phi(\beta) = \int_0^1 x^\beta \phi(x)dx , \tag{B1}$$

where β is the exponent of integral energy spectrum of primary (~ 1.8) and $\phi(x)$ the single particle distribution in the process of a nucleon-nucleon interaction. For instance, putting[35]

$$\phi(x) = \phi_0(1-x)^4/x \tag{B2}$$

we get

$$\Phi(\beta) = \phi_0\Gamma(\beta)\Gamma(5)/\Gamma(\beta+5) . \tag{B3}$$

Since $\Phi(1)$ corresponds to the average inelasticity $\langle K \rangle$ (~ 0.5), we get $\phi_0 = 5\langle K \rangle \sim 2.5$, leading to a result $\Phi(\beta = 1.8) \sim 0.133$. In the present work, we use Eq. (B2) in the case of analytical calculation for the flux of cosmic-ray secondaries, while an empirical form[9] of $\phi(x)$ closely reproducing accelerator data is used in the case of simulation.

Now, assuming the integral energy spectrum of protons at depth t as

$$I_p(E_0,t) = I_p^{(0)}E_0^{-\beta_p}e^{-t/\Lambda_p} , \tag{B4}$$

the number of charged pions with energy $(E, E + \Delta E)$ produced at depth $(t, t + \Delta t)$ is given by

$$\frac{2}{3}\int_E^\infty dE_0\frac{dI_p}{dE_0}\phi\left[\frac{E}{E_0}\right]\frac{\Delta E}{E_0}\frac{\Delta t}{\lambda_p}$$

$$= \langle n_{\pi^{\pm}} \rangle_p \frac{dI_p(E,t)}{dE}\frac{\Delta t}{\lambda_p}\Delta E \tag{B5}$$

with

$$\langle n_{\pi^{\pm}} \rangle_p = \frac{2}{3}\Phi(\beta_p) .$$

In Table VIII, we summarize the form of the production rate $\langle n_a \rangle_A$ for various combinations of primary A and secondary a. Here $\langle w \rangle_A$ is the rate of wounded nucleons inside the projectile nucleus A, produced by the collision with an air nucleus. Assuming the Glauber approximation,[21] it is expressed by Eq. (10) in the text. For instance, the magnitude of $\langle w \rangle_A$ varies approximately $\frac{2}{3}-\frac{1}{5}$ for $A = \alpha$–Fe. $P_{A\alpha}(A > \alpha)$ and $P_{AX}(A \geq X > \alpha)$ in Table VIII denote the average number of α and the fragmentation probability from A to X in the collision of nucleus A and air nucleus, respectively. In Table IX we summarize numerical values of P_{AX} obtained by Freier and Waddington.[36] In the case of simulation calculations, however, we used those parametrized by Tsao, Silberberg, and Letaw.[37] The cross sections mentioned above are presented in Appendix E.

With use of the production rate $\langle n_a \rangle_A$ summarized in Table VIII, we can express the flux of particle a originating from a cosmic-ray primary A, in a general form, as

TABLE IX. Numerical values of fragmentation probability P_{AX} obtained by Freier and Waddington. In the case of $X = \alpha$, it gives average number of α produced.

a \ A	L ($Z=3-5$)	M ($Z=6-9$)	LH ($Z=10-15$)	MH ($Z=16-19$)	VH ($Z=20-26$)
α	0.61 ± 0.11	0.72 ± 0.06	0.77 ± 0.10	1.17 ± 0.19	1.71 ± 0.10
L	0.11 ± 0.04	0.24 ± 0.03	0.21 ± 0.04	0.17 ± 0.05	0.24 ± 0.03
M		0.17 ± 0.02	0.39 ± 0.06	0.20 ± 0.06	0.17 ± 0.02
LH			0.16 ± 0.04	0.42 ± 0.09	0.22 ± 0.03
MH				0.06 ± 0.03	0.20 ± 0.02
VH					0.17 ± 0.02

TABLE X. Explicit expressions of $G_{A \to a}(t)$ for various combinations of a and A. Here, $G_0(x) = (e^x - 1)/x$, $G_1(x,y) = (e^x - e^y)/(x - y)$, and $G(x,y;z) = G_0(x) + z[G_0(x) - G_0(y)]/(x - y)$.

A	a	$G_{A \to a}(t)$	Variables
p	$\pi^{\pm}$	$G_0\left[\dfrac{t}{\Lambda_{p\pi}}\right] \simeq 1 + \dfrac{1}{2}\dfrac{t}{\Lambda_{p\pi}} + \cdots$	$\dfrac{1}{\Lambda_{Aa}} = \dfrac{1}{\Lambda_A} - \dfrac{1}{\Lambda_a}$
	γ, e	$\displaystyle\sum_{i=1}^{2} N_i(\beta_p) G_0\left[\dfrac{t}{\Lambda_{p\gamma,i}}\right] \simeq 1 + \dfrac{1}{2}\dfrac{t}{\Lambda_{p\gamma}} + \cdots$	$\dfrac{1}{\Lambda_{A,ab}} = \dfrac{1}{\Lambda_{Aa}} + \dfrac{1}{\Lambda_{Ab}}$
$A\,(\geq \alpha)$	$\pi^{\pm}$	$G_1\left[\dfrac{t}{\Lambda_{A\pi}}, \dfrac{t}{\Lambda_{Ap}}\right] \simeq 1 + \dfrac{1}{2}\dfrac{t}{\Lambda_{A,p\pi}} + \cdots$	$\dfrac{1}{\Lambda_\gamma(s)} = -\displaystyle\sum_{i=1}^{2} N_i(s)\lambda_i(s)$
	γ, e	$\displaystyle\sum_{i=1}^{2} N_i(\beta_A) G_1\left[\dfrac{t}{\Lambda_{A\gamma,i}}, \dfrac{t}{\Lambda_{Ap}}\right] \simeq 1 + \dfrac{1}{2}\dfrac{t}{\Lambda_{A,p\gamma}} + \cdots$	$\dfrac{1}{\Lambda_{A\gamma,i}} = \dfrac{1}{\Lambda_A} + \lambda_i(\beta_A)$
α	p, n	$G_0\left[\dfrac{t}{\Lambda_{\alpha p}}\right] \simeq 1 + \dfrac{1}{2}\dfrac{t}{\Lambda_{\alpha p}} + \cdots$	$\dfrac{1}{\lambda_{AA',X}} = P_{AA'} \cdot \dfrac{\langle n_X \rangle_{A'}}{\langle n_X \rangle_A} \dfrac{1}{\lambda_A}$
$A\,(> X)$	X $(p,n,\alpha,\ldots)$	$\displaystyle\sum_{A'} G\left[\dfrac{t}{\Lambda_{AX}}, \dfrac{t}{\Lambda_{AA'}}; \dfrac{t}{\lambda_{AA',X}}\right] \simeq 1 + \dfrac{1}{2}\dfrac{t}{\Lambda_{AX}^{*}} + \cdots$	$\dfrac{1}{\Lambda_{AX}^{*}} = \dfrac{1}{\Lambda_{AX}} + \displaystyle\sum_{A'} \dfrac{1}{\lambda_{AA',X}}$

$$I_{A \to a}(E,t) = \langle n_a \rangle_A \frac{t}{\lambda_A} G_{A \to a}(t) I_A(E,t) , \qquad (B6)$$

with

$$I_A(E,t) = I_A^{(0)} E^{-\beta_A} e^{-t/\Lambda_A} . \qquad (B7)$$

Here, we neglect secondaries coming from the collision of $\pi^{\pm}$ with air nuclei because of their small energy. λ_A and Λ_A are the collision and attenuation mean free paths, respectively. Here and in what follows, λ and Λ correspond always to collision and attenuation mean free paths.

$G_{A \to a}(t)$ equals unity at the top of the atmosphere, and depends generally on λ_A and Λ_A, and also on $\langle w \rangle_A$ and P_{AX} in the case $A \geq \alpha$. In Table X we summarize the explicit forms of $G_{A \to a}(t)$, where we define the following familiar functions in cascade theory:[38]

$$N_1(s) = M(s)\sqrt{s} + H_2(s)$$

and $\qquad\qquad\qquad\qquad\qquad\qquad (B8)$

$$N_2(s) = -M(s)\sqrt{s} + H_1(s) .$$

APPENDIX C: PROPAGATION OF FRAGMENTED NUCLEONS EMITTED FROM α

Let us put the integral flux of primary α at a level t as

$$I_\alpha(E,t) = I_\alpha^{(0)} E^{-\beta_\alpha} e^{-t/\lambda_\alpha} , \qquad (C1)$$

with

$$1/\Lambda_\alpha = (1 - P_{\alpha\alpha})/\lambda_\alpha . \qquad (C2)$$

Here, E is the energy per nucleon, and $P_{\alpha\alpha}$ the fragmentation probability of the process $\alpha \to \alpha$, 5–10% according to Freier and Waddington.[36] So, using $\lambda_\alpha = 48.85$ g/cm^2, expected from the formula of cross section given by

Hagen and Watts,[39] we get

$$\Lambda_\alpha = 51.5 \text{ g/cm}^2 . \qquad (C3)$$

Four nucleons are produced by the collision of α with an air target, among which w nucleons $(0 \leq w \leq 4)$ collide with nucleons inside the air nucleus (wounded nucleons), and the other $(4 - w)$ nucleons (spectator nucleons) are produced incoherently. We represent such a probability by $P_{w/\alpha}$.

Let the vertical intensity of nucleons originated in the above be $I_{\alpha \to N}(E,t)$, then the diffusion equation for such nucleons is now written as

$$\Delta I_{\alpha \to N} = -\frac{\Delta t}{\Lambda_N} I_{\alpha \to N}$$

$$+ \frac{\Delta t}{\lambda_\alpha} \sum_{w=0}^{4} P_{w/\alpha}\left[(4 - w)I_\alpha \right.$$

$$+ w \int_0^1 I_\alpha\left[\frac{E}{1-K}, t\right]$$

$$\left. \times \eta_N(K) dK \right] . \qquad (C4)$$

Here, $\Lambda_N \ (= \Lambda_p)$ denotes the absorption length of nucleons in air, and $\eta_N(K)$ the inelasticity distribution of nucleon. Putting $I_{\alpha \to N} \propto E^{-\beta_\alpha}$, Eq. (C4) is immediately rewritten as

$$\left[\frac{d}{dt} + \frac{1}{\Lambda_p}\right] I_{\alpha \to N} = \langle n_N \rangle_\alpha \frac{1}{\lambda_\alpha} I_\alpha ; \qquad (C5)$$

here,

$$\langle n_N \rangle_\alpha = 4\{ 1 - \langle w \rangle_\alpha [1 - \langle (1 - K_N)^{\beta_\alpha} \rangle] \}$$

$$\simeq 4\left[1 - \frac{\langle w \rangle_\alpha \lambda_p}{\Lambda_p} \right] \text{ for } \beta_p \simeq \beta_\alpha , \qquad (C6)$$

with

$$\langle (1-K_N)^{\beta_\alpha} \rangle = \int_0^1 (1-K)^{\beta_\alpha} \eta_N(K) dK \ , \tag{C7}$$

and

$$\langle w \rangle_\alpha = \tfrac{1}{4} \sum_{w=0}^4 w P_{w/\alpha} \ . \tag{C8}$$

$\langle w \rangle_\alpha$ corresponds to the average rate of wounded nucleons in the collision of α versus air nucleus, which is expressed under the Glauber approximation as Eq. (10) in the text.

The solution of Eq. (C5) is now given by

$$I_{\alpha \to N}(E,t) = \langle n_N \rangle_\alpha \frac{t}{\lambda_\alpha} G_{\alpha \to N}(t) I_\alpha(E,t) \ . \tag{C9}$$

The explicit form of $G_{\alpha \to N}(t)$ is summarized in Table X.

APPENDIX D: ZENITH-ANGLE DISTRIBUTION AND EFFECTIVE SOLID ANGLE

The effective solid angle at the top of the atmosphere is given, irrespective of the kind of primaries, by

$$\Omega = \int \int_{\Omega \leq 2\pi} \cos\theta \, d\Omega = \pi \tag{D1}$$

and the zenith-angle distribution is just the integrand of Eq. (D1). The term $\cos\theta$ is due to the horizontal setting of chamber.
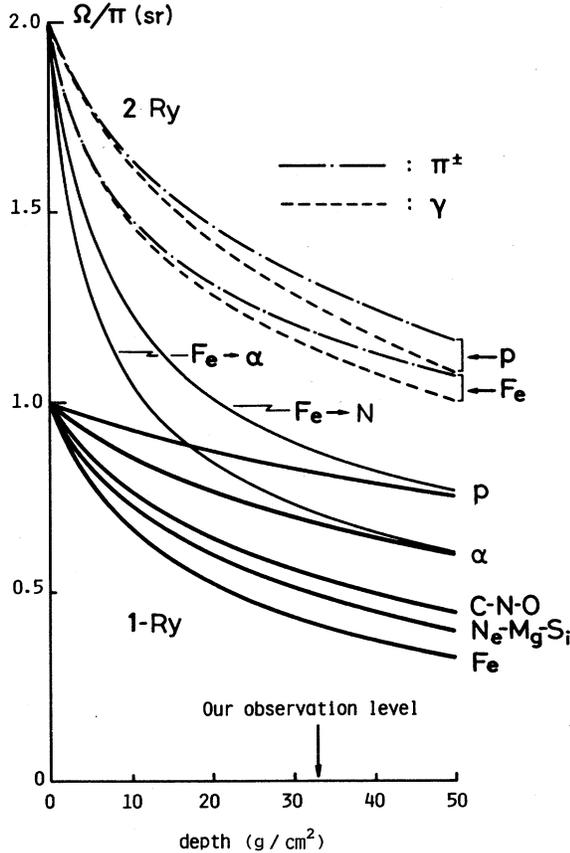

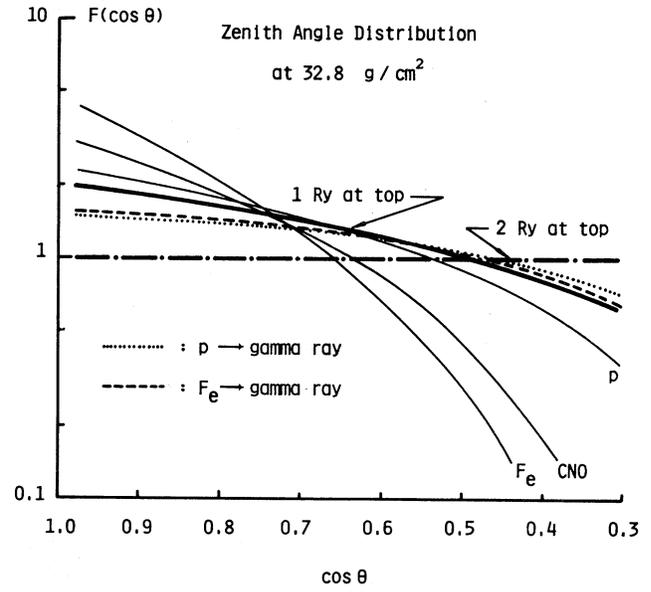FIG. 33. Altitude variation of effective solid angle for various primaries and secondaries.

FIG. 34. Zenith-angle distribution for various particles at our observation level.

Let us consider the effective solid angle at a level t for some observed particle a originating from a primary particle A. In the case of $A = a$, it is easily written as

$$\Omega_A(t) = \int \int_{\Omega \leq 2\pi} \omega_A(\cos\theta, t) \cos\theta \, d\Omega \ , \tag{D2a}$$

$$\omega_A(x,t) = \exp\left[-\frac{t}{\Lambda_A} \left[\frac{1}{x} - 1 \right] \right] \ . \tag{D2b}$$

In the case of $A \neq a$, remembering the vertical intensity summarized in Appendix B, we can express immediately, after replacing t by $t/\cos\theta$, as

$$\Omega_{A \to a}(t) = \int \int_{\Omega \leq 2\pi} \omega_{A \to a}(\cos\theta, t) d\Omega \ , \tag{D3a}$$

$$\omega_{A \to a}(x,t) = \omega_A(x,t) \frac{G_{A \to a}(t/x)}{G_{A \to a}(t)} \ . \tag{D3b}$$

In Fig. 33 we present the altitude variation of the effective solid angle for various kinds of particles.

Zenith-angle distribution are given by the integrands of Eqs. (D2a) and (D3a), and expressed as, taking account of the normalization

$$F_A(\cos\theta, t) d\Omega = \frac{\omega_A(\cos\theta, t)}{\Omega_A(t)} \cos\theta \, d\Omega \ , \tag{D4}$$

$$F_{A \to a}(\cos\theta, t) d\Omega = \frac{\omega_{A \to a}(\cos\theta, t)}{\Omega_{A \to a}(t)} d\Omega \ . \tag{D5}$$

In Fig. 34, we demonstrate the zenith-angle distribution for various particles at our observation level, which are necessary for the calculation of detection efficiency.

APPENDIX E: SIMULATION OF NUCLEAR INTERACTIONS INSIDE THE CHAMBER

As shown in Fig. 35 we sample an incidence point (x,y) on the plane S_{eff} first, and an incidence direction
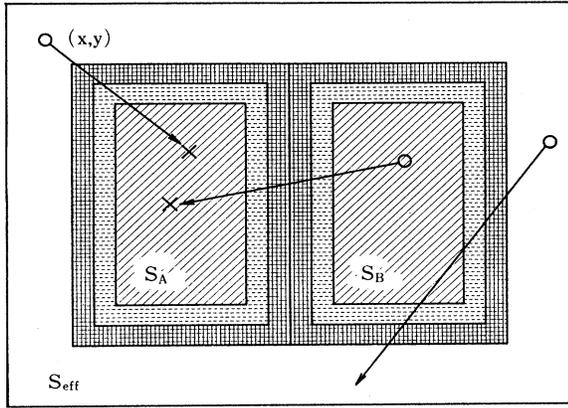
FIG. 35. Illustration of the top view of our chamber and examples of the sampling of cosmic-ray projectile.

FIG. 37. Relation between the average depth of the shower maximum $\langle T_{\max} \rangle$ and the initial energy $\sum E_\gamma$.

(θ, ϕ) second, according to Eqs. (D4) and (D5). If $\theta > \theta_c$, we omit such event in this step (however, we must count it in the total number of statistics N_0).

Third, we sample the first collision point in chamber, where we take into account exactly the configuration of the wooden and acrylic boxes (see Fig. 35). Collision cross sections for nucleon-nucleus interactions are interpolated among experimental data[40] as shown in Fig. 36,
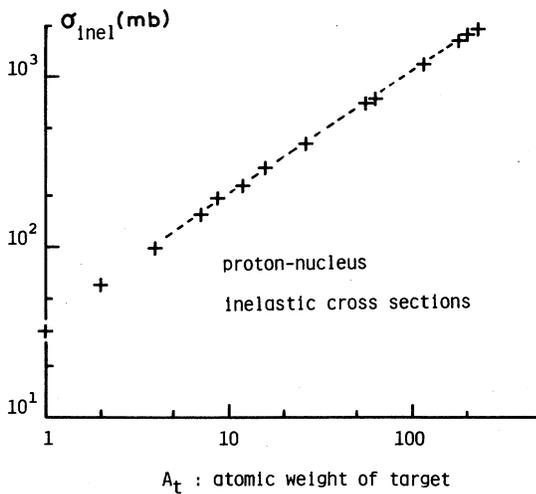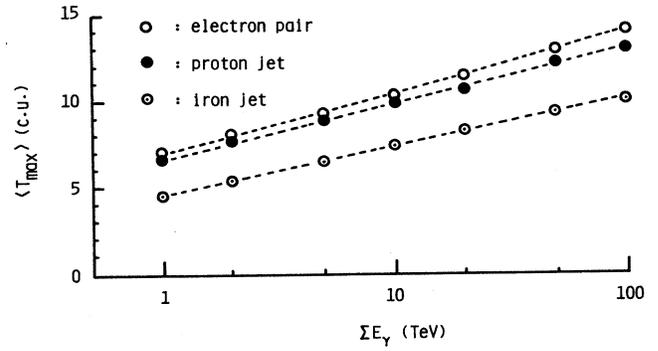
while in the case of nucleus-nucleus interactions, we use the Hagen-Watts formula[39]

$$\sigma_{AB} = \pi r_0^2 (A^{1/3} + B^{1/3} - \zeta)^2 ,\qquad \text{(E1)}$$

with

$$r_0 = 1.29 \times 10^{-13} \text{ cm} ,\qquad \text{(E2a)}$$

and

$$\zeta = 1.189 \exp[-0.054\,46 \min(A,B)] ,\qquad \text{(E2b)}$$

FIG. 36. Experimental data on the cross section of proton-nucleus collision. A dashed curve is used for the simulation calculation.

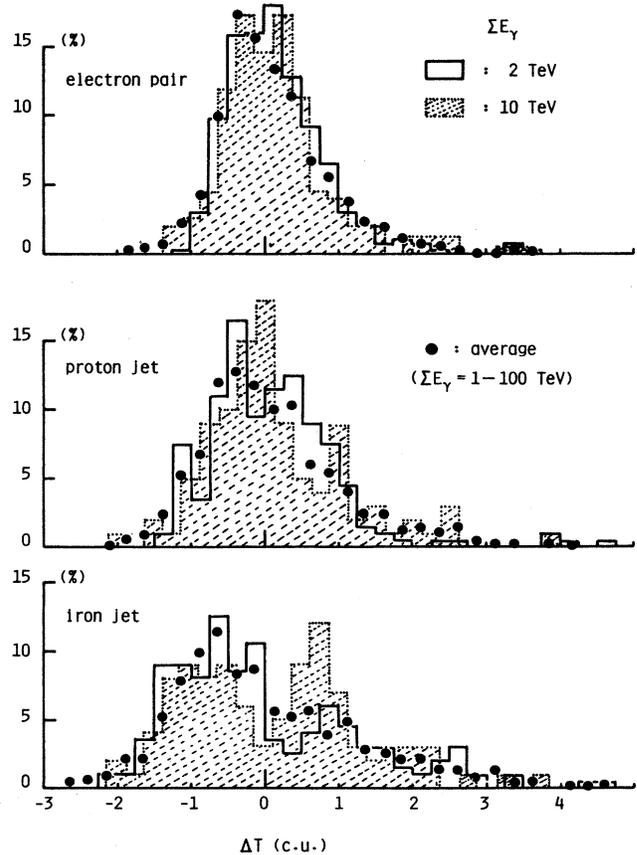FIG. 38. ΔT distribution obtained by simulations for three kinds of projectiles. A closed circle denotes the average result, obtained by superposing all energies 1–100 TeV.

here, A and B are the mass numbers of the projectile and target nuclei, respectively.

If the collision point is inside the chamber, we adopt it for the present, and subsequently perform the simulation of particle production, the details of which are given in Ref. 9. The average rate of wounded nucleons $\langle w \rangle_A$ is, however, determined by the Glauber formula Eq. (10) in text in this paper, and we assume its distribution as

$$\Xi_A(w)dw = g_A w^{g_A - 1} dw \quad \text{with} \quad g_A = \frac{\langle w \rangle_A}{1 - \langle w \rangle_A} \ . \quad \text{(E3)}$$

So, the number of wounded nucleons is given by

$$N_w = Aw \ . \quad \text{(E4)}$$

After performing the simulation of particle production according to Ref. 9, we get the energy $\sum E_\gamma$ released into γ-ray component. Here we take into account the error of the energy determination as shown in Fig. 16 in text. In this paper, we sample the energy $\sum E'_\gamma$ from the distribution

$$\frac{1}{\sqrt{2\pi}\sigma} e^{-Z^2/2\sigma^2} dZ \quad \text{with} \quad Z = \sum E'_\gamma \Big/ \sum E_\gamma - 1 \ , \quad \text{(E5)}$$

where σ depends on $\sum E_\gamma$ as presented in Fig. 16. In the following discussions, we put again $\sum E'_\gamma$ as $\sum E_\gamma$ for the sake of simplicity.

Since the selection condition for practical events is $\sum E_\gamma \geq 2$ TeV, we do not continue if the simulated event has a energy less than 2 TeV. If satisfying this criterion, we calculate the path length T_{path} to the separation point from the chamber.

Practically, we trigger events by dark-spot signals recorded successively on x-ray films, so that we should discard such an event that the maximum depth T_{max} of the electron shower goes beyond T_{path}, even though it clears all selection criteria mentioned so far.

As shown in Fig. 37, obtained from Fig. 9 in the text, the average depth of shower maximum $\langle T_{\text{max}} \rangle$ in transition of spot darkness depends slightly on shower energy as well as on the kind of primary.

T_{max} fluctuates greatly from event to event, and we defined

$$\Delta T = T_{\text{max}} - \langle T_{\text{max}} \rangle \quad \text{(E6)}$$

and checked its distribution with the use of simulations, as shown in Fig. 38. ΔT given here does not mean the penetration of hadron and/or γ in the heavy absorber usually defined (or interpreted) by emulsion-chamber experiments at mountain level, but merely fluctuation of electron shower development *event by event*. The justification of simulation calculations on fluctuation problems is discussed in Ref. 16.

One finds that the shape of the distribution does not depend so strongly on shower energy, but slightly on the kind of projectile. So we superposed histograms over all energies 1–100 TeV for each projectile, which are stored on disk.

Now, we sample ΔT according to the distribution thus obtained, and then we determine T_{max} from Eq. (E6), where $\langle T_{\text{max}} \rangle$ is given by Fig. 37. We adopt events satisfying $T_{\text{max}} < T_{\text{path}}$, or those such that the depth corresponding to $0.7D_{\text{max}}$ is within T_{path}; otherwise we discard them. Finally, we get the number of events N_{obs} clearing all selection criteria mentioned so far. Of course, we can get the conversion factor κ_γ simultaneously for each event.

[1]N. L. Grigorov, I. D. Rapoport, I. A. Savenko, V. E. Nesterov, and V. L. Prokhin, in *12th International Cosmic Ray Conference, Hobart, Tasmania, 1971*, edited by A. G. Fenton and K. B. Fenton (University of Tasmania Press, Hobart, Tasmania, 1971), Vol. 5, p. 1760.

[2]V. G. Abulova, L. A. Hein, K. V. Mandritskaya, G. P. Sazhina, N. V. Sazhina, N. V. Sokolskaya, E. S. Troshina, A. Ya. Varkovitskaya, E. A. Zamchalova, and V. I. Zatsepin, in *18th International Cosmic Ray Conference, Bangalore, India, 1983, Conference Papers*, edited by N. Durgaprasad *et al.* (Tata Institute of Fundamental Physics, Bombay, 1983), Vol. 9, p. 179.

[3]T. H. Burnett *et al.*, Nucl. Instrum. Methods A251, 583 (1986).

[4]M. Ryan, J. F. Ormes, and V. K. Balasubrahmanyan, Phys. Rev. Lett. 28, 985 (1972).

[5]Fuji-Kanbala ECC group, Ren *et al.*, Phys. Rev. D 38, 1404 (1988); 38, 1417 (1988); 38, 1426 (1988).

[6]For example, B. V. Sreekantan, in *16th International Cosmic Ray Conference, Kyoto, 1979, Conference Papers* (Institute of Cosmic Ray Research, University of Tokyo, Tokyo, Japan, 1979), Vol. 14, p. 345.

[7]T. H. Burnett *et al.*, in *Proceedings of the 19th International Cosmic Ray Conference, La Jolla, California, 1985*, edited by F. C. Jones, J. Adams, and G. M. Mason (NASA Conf. Publ. 2376) (Goddard Space Flight Center, Greenbelt, MD, 1985),

Vol. 2, p. 48.

[8]J. M. Grunsfeld, J. L'Heureux, P. Meyer, D. Muller, and S. P. Swordy, Astrophys. J. 327, 31 (1988).

[9]Y. Niihori, T. Shibata, I. M. Martin, E. H. Shibuya, and A. Turtelli, Jr., Phys. Rev. D 36, 783 (1987).

[10]T. Fujinaga, M. Ichimura, Y. Niihori, and T. Shibata, Nucl. Instrum. Methods A276, 317 (1989).

[11]J. Nishimuara *et al.*, in *Proceedings of the 19th International Cosmic Ray Conference* (Ref. 7), Vol. 6, p. 12.

[12]M. Ichimura, K. Kirii, and T. Shibata, in *Proceedings of Balloon Symposium*, edited by J. Nishimura (Institute of Space and Astronautical Science, Tokyo, Japan, 1987), p. 128.

[13]P. H. Fowler and D. H. Perkins, Philos. Mag. 46, 587 (1955).

[14]For example, M. Fujii, J. Nishimura, and T. Kobayashi, Nucl. Instrum. Methods 226, 496 (1984).

[15]K. Teraoka, K. Toda, H. Nanjyo, S. Mase, H. Matsutani, S. Kawaguchi, H. Koseki, Y. Kawamura, M. Ichimura, T. Kobayashi, T. Shibata, Y. Niihori, and Y. Yoshizumi, in *Proceedings of Balloon Symposium* (Ref. 12), pp. 115 and 120.

[16]M. Okamoto and T. Shibata, Nucl. Instrum. Methods A257, 155 (1987).

[17]N. Hotta, N. Munakata, M. Sakata, Y. Yamamoto, S. Dake, H. Ito, M. Miyanishi, K. Kasahara, T. Yuda, K. Mizutani, and I. Ohta, Phys. Rev. D 22, 1 (1980); Nuovo Cimento 70A, 73 (1982).

[18]T. Shibata *et al.*, in *Proceedings of the 17th International Cosmic Ray Conference,* Paris, France, 1981 (Centre d'Etudes Nucleaires Saclay, Gif-sur-Yvette, 1981), Vol. 5, pp. 214, 218, and 222; K. Kasahara, Phys. Rev. D **31**, 2737 (1985); see also Ref. 17.

[19]I. Ohta *et al.*, Nucl. Instrum. Methods **161**, 35 (1979).

[20]Private discussions with K. Kasahara.

[21]R.J. Glauber, in *Lectures in Theoretical Physics,* edited by W. E. Britten and L. G. Dunham (Interscience, New York, 1959), Vol. 1, p. 315.

[22]E. Konishi, T. Shibata, E. H. Shibuya, and N. Tateyama, Prog. Theor. Phys. **56**, 1845 (1976).

[23]M. Fuki, Matsusho-Gakuen University Report No. 390-12, 1987, p. 137 (unpublished).

[24]K. Kinoshita, A. Minaka, and H. Sumiyoshi, Prog. Theor. Phys. **61**, 165 (1979).

[25]J. Nishimura, M. Fujii, E. Aizu, H. Hiraiwa, T. Kobayashi, K. Niu, I. Ohta, R. L. Golden, T. A. Koss, J. J. Lord, and R. J. Wilkes, Astrophys. J. **238**, 394 (1980); J. Nishimura *et al.*, in *Proceedings of Balloon Symposium* (Ref. 12), p. 162.

[26]K. Murakami *et al.*, in *Proceedings of the 15th International Cosmic Ray Conference,* Plovdiv, Bulgaria, 1977, edited by B. Beter (Institute for Nuclear Research and Nuclear Energy, Sofia, 1977), Vol. 6, p. 143.

[27]K. Kondo, Invited talk at the meeting of the Physical Society of Japan held at Ehime University, Matsuyama, Japan, 1988.

[28]T. H. Burnett *et al.*, in *Proceedings of the 20th International Cosmic Ray Conference,* Moscow, USSR, 1987, edited by V.

A. Kozyarivsky *et al.* (Nauka, Moscow, 1987), Vol. 5, p. 185.

[29]M. Lohrmann, P. Sain, and M. Teucher, Phys. Rev. **115**, 654 (1959).

[30]P. Fowler and C. J. Waddington, Philos. Mag. **1**, 637 (1956).

[31]M. Simon *et al.*, Astrophys. J. **237**, 712 (1980).

[32]E. Juliusson *et al.*, in *18th International Cosmic Ray Conference, Bangalore, India, 1983, Conference Papers* (Ref. 2), Vol. 2, p. 21.

[33]R. Pinkau, U. Pollvogt, W. R. H. Schmidt, and R. W. Hugget, in *Proceedings of the 11th International Cosmic Ray Conference,* Hungary, 1969, edited by P. Gombás, Acta Phys. Acad. Sci. Hung. Suppl. **1**, 291 (1970).

[34]M. Niwa, M. Ichimura, Y. Eguchi, T. Fujinaga, and Y. Horiguchi, Institute for Cosmic Ray Research Report No. ICR-50-85-4, University of Tokyo, 1985 (unpublished).

[35]F. E. Taylor *et·al.*, Phys. Rev. D **14**, 1217 (1976).

[36]P. S. Freier and C. J. Waddington, Astrophys. Space Sci. **38**, 419 (1975).

[37]C. H. Tsao, R. Silberberg, and J. R. Letaw, in *18th International Cosmic Ray Conference, Bangalore, India, 1983, Conference Papers* (Ref. 2), Vol. 2, p. 194.

[38]For example, B. Rossi and K. I. Greisen, Rev. Mod. Phys. **13**, 240 (1941); J. Nishimura, in *Handbuch der Physik,* edited by S. Rügge (Springer, Berlin, 1964), Vol. 46/2, p. 1.

[39]F. A. Hagen *et al.*, Astrophys. J. **212**, 262 (1977).

[40]Particle Data Group, C. G. Wohl *et al.*, Rev. Mod. Phys. **56**, S53 (1984).